

Stellar kinematics of X-ray bright massive elliptical galaxies ^{*}

N. Lyskova,^{1,2} E. Churazov,^{1,2} A. Moiseev,^{3,4} O. Sil’chenko,^{4,5} I. Zhuravleva^{6,7}

¹ *Max-Planck-Institut für Astrophysik, Karl-Schwarzschild-Strasse 1, 85741 Garching, Germany*

² *Space Research Institute (IKI), Profsoyuznaya 84/32, Moscow 117997, Russia*

³ *Special Astrophysical Observatory, Russian Academy of Sciences, Nizhnii Arkhyz, Karachaevo-Cherkesskaya Republic, 369167 Russia*

⁴ *Sternberg Astronomical Institute, M. V. Lomonosov Moscow State University, Moscow, 119992 Russia*

⁵ *Isaac Newton Institute of Chile, Moscow Branch*

⁶ *Kavli Institute for Particle Astrophysics and Cosmology, Stanford University, 452 Lomita Mall, Stanford, CA 94305-4085, USA*

⁷ *Department of Physics, Stanford University, 382 Via Pueblo Mall, Stanford, CA 94305-4060, USA*

11 April 2014

ABSTRACT

We discuss a simple and fast method for estimating masses of early-type galaxies from optical data and compare the results with X-ray derived masses. The optical method relies only on the most basic observables such as the surface brightness $I(R)$ and the line-of-sight velocity dispersion $\sigma_p(R)$ profiles and provides an anisotropy-independent estimate of the galaxy circular speed V_c . The mass-anisotropy degeneracy is effectively overcome by evaluating V_c at a characteristic radius R_{sweet} defined from local properties of observed profiles. The sweet radius R_{sweet} is expected to lie close to R_2 , where $I(R) \propto R^{-2}$, and not far from the effective radius R_{eff} . We apply the method to a sample of five X-ray bright elliptical galaxies observed with the 6-m telescope BTA-6 in Russia. We then compare the optical V_c -estimate with the X-ray derived value, and discuss possible constraints on the non-thermal pressure in the hot gas and configuration of stellar orbits. We find that the average ratio of the optical V_c -estimate to the X-ray one is equal to ≈ 0.98 with 11% scatter, i.e. there is no evidence for the large non-thermal pressure contribution in the gas at $\sim R_{\text{sweet}}$. From analysis of the Lick indices $H\beta$, Mgb , $Fe5270$ and $Fe5335$, we calculate the mass of the stellar component within the sweet radius. We conclude that a typical dark matter fraction inside R_{sweet} in the sample galaxies is $\sim 60\%$ for the Salpeter IMF and $\sim 75\%$ for the Kroupa IMF.

Key words: Galaxies: Kinematics and Dynamics, X-Rays: Galaxies

1 INTRODUCTION

Being the most massive galaxies in the local Universe, giant elliptical galaxies provide a natural laboratory to study galaxy formation, assembly and evolution processes. The current paradigm of galaxy formation is the hierarchical sce-

nario which suggests that early-type galaxies have complex merging histories of assembling most of the mass through accretion of small galaxies with rare major merger events (e.g. de Lucia and Blaizot 2007; Naab et al. 2007). Accurate mass determinations and disentangling a luminous and dark matter components at different redshifts are the key steps towards a consistent theory for elliptical galaxies formation.

Determining the mass profile of early-type galaxies is a notoriously difficult problem as there are no dynamical tracers with the known intrinsic shape and structure of orbits, so that circular velocity curves of elliptical galaxies cannot

^{*} Based on observations obtained with the 6-m telescope of the Special Astrophysical Observatory of the Russian Academy of Sciences. The observations were carried out with the financial support of the Ministry of Education and Science of Russian Federation (contracts no. 16.518.11.7073 and 14.518.11.7070).

be measured directly. A number of methods are in use for constraining the mass of early-type galaxies and the shape of dark matter halos, each having its own set of assumptions and limitations. Comparison of the mass profiles obtained from different independent techniques is necessary to get reliable estimates. It also helps to control the systematic uncertainties, inherent in all methods, as well as leads to interesting constraints on properties of elliptical galaxies.

One of the mass estimation techniques comes from X-ray observations of extended hot X-ray-emitting coronae of massive elliptical galaxies. It is a powerful tool to probe the mass distribution over several decades in radius: from $\sim 0.1R_{\text{eff}}$ out to $\sim 10R_{\text{eff}}$. In this approach spherical symmetry of a galaxy and hydrostatic equilibrium of the gas are commonly assumed. While the spherical symmetry approximation introduces only a small bias, if any (e.g. Piffaretti et al. 2003; Buote and Humphrey 2012c), validity of the hydrostatic equilibrium assumption is the subject of debate. When one is able to quantify deviations from hydrostatic equilibrium, it allows to estimate (although indirectly) pressure of the non-thermal gas motions. Most simulations suggest that in relaxed systems hydrostatic approximation works well, with non-thermal support at the level of 5% to 35% of the total gas pressure (e.g. Nagai, Vikhlinin and Kravtsov 2007). When X-ray observations are combined with, for instance, optical data on the stellar kinematics, then comparison between the X-ray gravitating mass profile and the optical mass allows one to estimate the magnitude of the non-thermal motions of the hot gas, to constrain the mass-to-light ratio, to disentangle stellar and dark matter contributions to the total gravitating mass profile and to characterize the distribution of stellar orbits.

Although elliptical galaxies suffer from a lack of ‘ideal’ traces like disc rotation curves in spiral galaxies and there is an inherent degeneracy between anisotropy and mass, studies of stellar kinematics and dynamics provide the tools for measuring the gravitating mass profile with sufficient accuracy (up to $\sim 15\%$, Thomas et al. 2005). Methods based on the Schwarzschild modeling of stellar orbits in axisymmetric (or even triaxial) potentials are considered to be the state-of-the-art techniques in this field. The most sophisticated approaches operate with full information on the line-of-sight velocity distribution including higher-order moments. The orbit-based methods allow to infer not only the total mass profile, but also to measure the dark matter content, derive mass-to-light ratios and get the distribution function of stellar orbits. Among the drawbacks of these methods are the high computational cost and the necessity to have high-quality observational data. So only nearby elliptical galaxies can be studied by means of Schwarzschild modelling, and for a large sample of objects, especially with noisy photometric and/or kinematical data, such an approach is not justified.

In this paper we discuss a simple approach for estimating the mass from the stellar kinematics (Churazov et al. 2010; Lyskova et al. 2012) that relies only on the most basic observables such as the surface brightness and line-of-sight velocity dispersion profiles. By design the method is simple and fast and has a modest scatter ($\Delta V_c/V_c \sim 5 - 10\%$, Lyskova et al. 2012). This makes it suitable for large samples

of elliptical galaxies even with limited and/or noisy observational data. Of course, the method is not intended to replace a thorough investigation of each individual galaxy.

We apply the method to a small and rather arbitrarily selected sample of massive elliptical galaxies located at the centers of groups and clusters, and bright in X-rays. The surface brightness and projected velocity dispersion profiles up to several effective radii have been measured with optical long-slit spectroscopic facilities on the 6-m telescope of the Special Astrophysical Observatory of the Russian Academy of Sciences (SAO RAS). Using publicly available Chandra data we also derive the X-ray mass profile and compare it with simple optical estimates.

The paper is organized as follows. In Section 2, we provide a brief description of the method. We apply it to real elliptical galaxies in Section 3, starting with the illustration of the method on the example of the extensively studied giant elliptical galaxy M87 in Section 3.1. Details on the observations of the sample of early-type galaxies are presented in Section 3.2. We derive circular speed estimates from optical and X-ray analyses and estimate stellar contributions in Section 3.3. Results are summarized in Section 4, and Section 5 contains conclusions.

2 DESCRIPTION AND JUSTIFICATION OF THE METHOD

Recent studies of massive elliptical galaxies based on different approaches (stellar dynamical methods, weak and strong lensing, hydrostatic mass modeling, and their combinations) suggest that the gravitational potential $\Phi(r)$ is close to isothermal (e.g. Gerhard et al. 2001; Treu et al. 2006; Koopmans et al. 2006; Fukazawa et al. 2006; Churazov et al. 2010). For a singular isothermal sphere the gravitational potential can be written as $\Phi(r) = V_c^2 \ln(r)$, the circular velocity curve is flat, $V_c(r) = \text{const}$, and the mass profile scales as $M(r) \propto r$. So if the total gravitational potential of the galaxy is indeed isothermal, it can be characterized with a single parameter - the circular speed V_c . Therefore to the first approximation it is sufficient to determine V_c at any radius and the task is to identify the radius at which the circular speed can be measured most accurately.

Stars in early-type galaxies can be considered as a collisionless system immersed in a gravitational field. Let us consider a spherical galaxy in the equilibrium state. Stars in such systems obey the Jeans equations which in the spherical coordinates (r, θ, ϕ) can be simply written as

$$\frac{d}{dr} j \sigma_r^2 + 2 \frac{\beta}{r} j \sigma_r^2 = -j \frac{d\Phi}{dr} = -j \frac{GM(r)}{r}, \quad (1)$$

where $j(r)$ ¹ is the stellar number density, $\sigma_r(r)$ is the radial velocity dispersion (weighted by luminosity),

$\beta(r) = 1 - \frac{\sigma_\phi^2 + \sigma_\theta^2}{2\sigma_r^2}$ is the stellar anisotropy parameter,

¹ Throughout this paper we denote a projected 2D radius as R and a 3D radius as r .

$M(r)$ is the total mass profile². The anisotropy $\beta(r)$ reflects the distribution of stellar orbits. If all stars in a galaxy are on circular orbits, then $\beta \rightarrow -\infty$, for pure radial orbits $\beta = 1$, and $\beta = 0$ for isotropic distribution of orbits.

We can link the unobservable quantities $j(r)$, $\beta(r)$ and $\sigma_r(r)$ with observable ones - a surface brightness $I(R)$ and a line-of-sight velocity dispersion $\sigma_p(R)$ profiles - via the following equations:

$$I(R) = 2 \int_R^\infty \frac{j(r)r dr}{\sqrt{r^2 - R^2}}, \quad (2)$$

$$\sigma_p^2(R) \cdot I(R) = 2 \int_R^\infty j(r)\sigma_r^2(r) \left(1 - \frac{R^2}{r^2}\beta(r)\right) \frac{r dr}{\sqrt{r^2 - R^2}}. \quad (3)$$

Nevertheless, the set of equations (1)-(3) is not closed. An inherent mass-anisotropy degeneracy does not allow us to solve it for the mass $M(r)$ and anisotropy $\beta(r)$ profiles simultaneously. Traditionally the degeneracy is overcome by assuming some parametric form of the mass or anisotropy profiles and fitting the resulting models to the observed $I(R)$ and $\sigma_p(R)$. However, both $M(r)$ and $\beta(r)$ are still poorly constrained from observational data alone (i.e., $I(R)$ and $\sigma_p(R)$) without resorting to the state-of-the-art modeling or adding detailed information on the line profiles. Here we discuss a technique that allows to estimate the mass of a galaxy without a priori parametrization of $M(r)$ and/or $\beta(r)$.

Assuming the logarithmic (isothermal) form of the gravitational potential $\Phi(r) = V_c^2 \ln(r) + \text{const}$ one can solve analytically the spherical Jeans equation coupled with equations (2)-(3) for three types of tracers' orbits - isotropic ($\beta = 0$), radial ($\beta = 1$) and circular ($\beta \rightarrow -\infty$). Note that for a typical stellar distribution $j(r)$ the projected velocity dispersion profile $\sigma_p(R)$ behaves differently depending on the value of β . In case of pure radial stellar orbits $\sigma_p(R)$ rapidly declines with the projected radius R , for the isotropic distribution of orbits $\sigma_p(R)$ declines much slower and, finally, $\sigma_p(R)$ increases with R for the circular orbits (e.g. Richstone and Tremaine 1984; Churazov et al. 2010, Figure 3). So there is an 'optimal radius' where the projected velocity dispersion profiles for different values of anisotropy (almost) intersect each other. The existence of such a radius is discussed in Richstone and Tremaine (1984), Gerhard (1993). The method based on this observation is presented in detail in Churazov et al. (2010) and Lyskova et al. (2012).

It is practical to express the circular speed in terms of the observable surface brightness and line-of-sight velocity dispersion profiles. For the logarithmic form of the gravitational potential $\Phi(r) = V_c^2 \ln(r)$ the circular velocity V_c profiles for isotropic, radial and circular orbits are given by Churazov et al. (2010):

$$\begin{aligned} V_c^{\text{iso}} &= \sigma_p(R) \sqrt{1 + \alpha + \gamma} \\ V_c^{\text{circ}} &= \sigma_p(R) \sqrt{2 \frac{1 + \alpha + \gamma}{\alpha}} \\ V_c^{\text{rad}} &= \sigma_p(R) \sqrt{(\alpha + \gamma)^2 + \delta - 1}, \end{aligned} \quad (4)$$

² Here we treat stars as test particles in the gravitational field $\Phi(r)$.

where

$$\alpha \equiv -\frac{d \ln I(R)}{d \ln R}, \quad \gamma \equiv -\frac{d \ln \sigma_p^2}{d \ln R}, \quad \delta \equiv \frac{d^2 \ln [I(R)\sigma_p^2]}{d(\ln R)^2}. \quad (5)$$

Often the subdominant terms γ and δ can be neglected, i.e. the dispersion profile is assumed to be flat and the curvature of $I(R)$ to be small, and equations (4) are simplified to:

$$\begin{aligned} V_c^{\text{iso}} &= \sigma_p \sqrt{\alpha + 1} \\ V_c^{\text{circ}} &= \sigma_p \sqrt{2 \frac{\alpha + 1}{\alpha}} \\ V_c^{\text{rad}} &= \sigma_p \sqrt{\alpha^2 - 1}. \end{aligned} \quad (6)$$

Let us call a 'sweet spot' R_{sweet} the radius at which all three curves $V_c^{\text{iso}}(R)$, $V_c^{\text{circ}}(R)$ and $V_c^{\text{rad}}(R)$ are very close to each other. At this radius the circular speed uncertainty due to the unknown stellar anisotropy is minimal. From the equations (6) it is clear that for $\alpha = 2$ the relation between V_c and σ_p is the same for all types of orbits. So in the general case the sweet spot is expected to be located not far from the radius R_2 where the surface brightness declines as R^{-2} which is in turn close to the half-light radius R_{eff} (see also Wolf et al. 2010). If $I(R) \propto R^{-2}$ over some range of radii $[R_1, R_2]$, then the estimates based on equations (4) or (6) should work well over the whole range $[R_1, R_2]$.

While the derivation of equations (4), (6) relies on the assumption of a flat circular velocity profile, it works well even in case of slowly varying $V_c(r)$. Lyskova et al. (2012) have tested the method on a sample of cosmological simulations of elliptical galaxies from Oser et al. (2010) and have shown that the circular speed can be recovered to a reasonable accuracy. The rms-scatter in the circular velocity estimate has been found to be 5.4% for present-day simulated massive elliptical galaxies without signs of significant rotation, while the sample averaged bias is less than 1%.

2.1 Rotation of galaxies.

Elliptical galaxies can be divided into two broad families: (1) normal ellipticals, which show significant rotation, tend to be flattened and have an oblate-spheroidal shape; and (2) giant ellipticals, which are almost non-rotating, less flattened and tend to be triaxial (e.g. Kormendy et al. 2009; Emsellem et al. 2007). Strictly speaking, the method in its original form is applicable only to non-rotating spherical galaxies, i.e. to no real ellipticals. Nevertheless, as tests on simulated galaxies show, the method still allows to recover the circular speed for massive elliptical galaxies without signs of significant rotation. For galaxies with rotational support the value of V_c derived from the observed $\sigma_p(R)$ using equations (4) or (6) will be likely underestimated. Can we reduce a bias arising from rotation to extend the method on fast-rotating elliptical galaxies?

Let us consider a disk rotating with the velocity $\tilde{V}_{\text{rot}}(R)$. When observed at an inclination angle i , where $i = 0^\circ$ corresponds to a face-on projection, the observed rotation velocity along an apparent major axis is simply $V_{\text{rot}}(R) =$

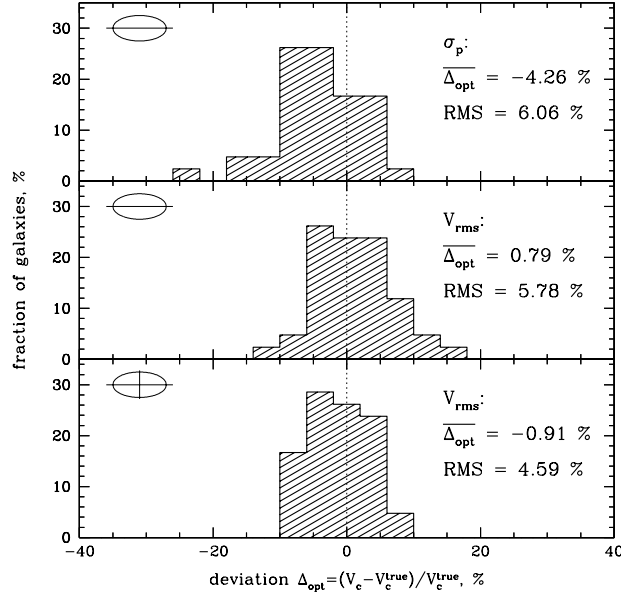


Figure 1. The fraction of galaxies (in %) as a function of deviation $\Delta_{opt} = (V_c^{iso} - V_c^{true}) / V_c^{true}$ for the sample of simulated galaxies with $\sigma_p(R_{eff}) > 150 \text{ km s}^{-1}$. Each galaxy is analysed for a set of random projections. For each projection the values of $I(R)$, $\sigma_p(R)$ and $V_{rot}(R)$ are calculated. The resulting V_c -estimates for all possible inclination angles for each galaxy are averaged. The black histogram in the upper panel results from ‘traditional’ analysis of $I(R)$ and $\sigma_p(R)$ profiles measured along a slit that is aligned with a major axis of a galaxy without taking into account $V_{rot}(R)$. In this case the V_c -estimate when averaged over the sample is biased low. The bias could be compensated when considering $V_{rms}(R) = \sqrt{\sigma_p(R) + V_{rot}(R)}$ instead of $\sigma_p(R)$ in equations (4), which is shown in the middle panel. The histogram in the lower panel shows V_c -estimates, when profiles along major and minor axes are available and V_{rms} is used. The averaged over the sample estimate is almost unbiased, the distribution looks roughly symmetric and the rms-scatter is moderate.

$\tilde{V}_{rot}(R) \sin i$. After averaging over different inclination angles $0 \leq i \leq \pi/2$ we get

$$\langle V_{rot}^2 \rangle = \int_0^{\pi/2} V_{rot}^2 \cos i \, di = \int_0^{\pi/2} \tilde{V}_{rot}^2 \sin^2 i \cos i \, di = \frac{1}{3} \tilde{V}_{rot}^2. \quad (7)$$

Thus the true rotation velocity is $\sqrt{3}$ times larger than the sample averaged observed velocity. This relation is similar to the relation between the simple V_c -estimate and the observed projected velocity dispersion near the sweet point (eq. 6, $\alpha = 2$). As the conversion coefficient at the sweet point does not (strongly) depend on the unknown configuration of stellar orbits, one can use the quantity $V_{rms}^2(R) = \sigma_p^2(R) + V_{rot}^2(R)$ (rms-speed), where $V_{rot}(R)$ is the observed rotation velocity, instead of $\sigma_p(R)$ in equation (4) or (6) to estimate the circular speed of a sample of galaxies that includes also fast rotators. It is clear that for oblate rotating galaxies the V_c inferred from V_{rms} is overestimated for the edge-on view and underestimated when the disk is viewed face-on. But after averaging over different inclination angles the bias disappears. The conjecture on using V_{rms} instead of $\sigma_p(R)$ in equation (4) or (6) has been further tested on a sample of resimulated galaxies from the high-resolution cosmological simulations of Oser et al. (2010). The sample includes both fast and slow rotators in a proportion that is generally consistent with findings of ATLAS^{3d} project (Emsellem et al. 2007, 2011; Naab et al. 2013).

First, for each simulated galaxy in the sample we mea-

sure the surface brightness, projected velocity dispersion and rotational velocity profiles along the apparent major axis of the galaxy, mimicking long-slit observations. Then we estimate the circular speed in two ways: 1) using information about $\sigma_p(R)$ (eq. 4) and 2) using $V_{rms}(R) = \sqrt{\sigma_p^2(R) + V_{rot}^2(R)}$ instead of $\sigma_p(R)$. As a next step we calculate the average deviation Δ_{opt} of the estimated circular speed from the true one $V_c^{true}(r) = \sqrt{GM(<r)}/r$, after averaging over all possible inclination angles. We consider only galaxies with the value of the projected velocity dispersion at the effective radius $\sigma_p(R_{eff})$ greater than 150 km s^{-1} (when the galaxy is viewed edge-on). The sample consists of 26 objects. The results of the analysis are presented in the form of histograms (fraction of galaxies versus deviation of the V_c -estimate from the true value) in Figure 1. In the upper panel of Figure 1 we show the histogram for the case when rotation is neglected. On average V_c is underestimated by $\Delta_{opt} = -4.3\%$. If we substitute $\sigma_p(R)$ with $V_{rms}(R) = \sqrt{\sigma_p^2(R) + V_{rot}^2(R)}$ then we get almost unbiased (within statistical errors) estimate of the circular speed with rms-scatter of $\approx 6\%$ (the middle panel of Figure 1). While for oblate ellipticals observations along the major axis carry all information needed for simple mass estimation, for triaxial galaxies rotation along the apparent minor axis might be significant. In a case when information is available along major and minor axes of a galaxy,

using $V_{\text{rms}}^2 = \frac{I_1 V_{\text{rms},1}^2 + I_2 V_{\text{rms},2}^2}{I_1 + I_2}$ makes the distribution of $\Delta_{\text{opt}} = (V_c - V_c^{\text{true}})/V_c^{\text{true}}$ more symmetric than for the ‘one slit’ case and reduces the rms-scatter down to 4.6% (lower panel of Figure 1). Note, that for the sample consisting of oblate rotating galaxies only there is no sense to use the weighted rms-speed $V_{\text{rms}}^2 = \frac{I_1 V_{\text{rms},1}^2 + I_2 V_{\text{rms},2}^2}{I_1 + I_2}$ as it leads to the underestimated value of V_c (compare the averaged deviations in the middle and lower panels). But for the sample containing also triaxial halos this approach helps to reduce the scatter and does not strongly bias the V_c -estimate. At least, for our sample of 26 simulated objects the bias is not significant, i.e., $\overline{\Delta_{\text{opt}}} < \text{RMS}/\sqrt{N}$.

2.2 An algorithm for estimating V_c

Based on the results of Lyskova et al. (2012) and the arguments presented in the previous section, the following algorithm has been developed:

(i) Calculate the logarithmic derivatives α , γ and δ from the observed surface brightness $I(R)$ and line-of-sight velocity dispersion $\sigma_p(R)$ profiles using equations (5).

(ii) Calculate the circular speed $V_c(R)$ for isotropic, radial and circular stellar orbits using equations (4) in the case of reliable data (full analysis) or equations (6) in the case of poor or noisy observational data (simplified analysis). For rotating galaxies use $V_{\text{rms}}(R)$ instead of $\sigma_p(R)$ in equations (4) or (6).

(iii) Estimate V_c as $V_c^{\text{iso}}(R_{\text{sweet}})$ at the sweet spot R_{sweet} - the radius at which all three curves $V_c^{\text{iso}}(R)$, $V_c^{\text{circ}}(R)$ and $V_c^{\text{rad}}(R)$ are maximally close to each other. At R_{sweet} the sensitivity of the method to the anisotropy parameter β is believed to be minimal so the estimation of the circular speed at this particular point is not affected much by the unknown distribution of stellar orbits.

3 ANALYSIS

3.1 M87, revisited. Illustration of the Method

In this section we illustrate all the steps of the described algorithm on one massive galaxy - M87 (NGC4486). M87 is a nearby (16.1 Mpc) giant elliptical galaxy, luminous in X-rays. It’s mass profile has been investigated in detail by a variety of methods. A technique analogous to the one described in Section 2.2 has already been applied to M87 (Churazov et al. 2010). However, new data on stellar kinematics warrant a reanalysis of the data.

Since the 1960s M87 has been extensively explored and there is a large amount of observational data. We focus here on a recent work by Murphy et al. (2011) (hereafter ‘M11’), who estimated M87’s mass profile from axisymmetric orbit-based modeling and compared the resulting total enclosed mass profile with other mass estimates available in the literature.

Schwarzschild modeling (Schwarzschild 1979) is considered to be a state-of-the-art method for dynamical investigation of nearby galaxies which allows one to re-

cover masses and orbital anisotropies with $\sim 15\%$ accuracy (Thomas et al. 2005). This technique consists in analysis of the three-dimensional orbital structure of a stellar system in an assumed gravitational potential and representation of the observed photometric and kinematic data by a superposition of constructed orbits. The system is assumed to be in dynamical equilibrium and as a rule to be viewed edge-on (e.g. Gebhardt et al. 2000, 2003; Thomas et al. 2004, 2005).

We assume that the mass and circular speed profiles for M87 derived in M11 are accurate and unbiased (as significant inherent systematic uncertainties are not expected to be in dynamical models (e.g. Thomas et al. 2007)) and compare our simple estimates with these curves.

For the analysis we use the same set of data as in M11. Namely, the stellar surface brightness profile comes from Kormendy et al. (2009), the stellar kinematic data come from the publicly available SAURON data set (Emsellem et al. 2004) and from M11 (VIRUS-P instrument).

We first compute the auxiliary coefficients α , γ and δ (eq. 5) from the smoothed $I(R)$ and $\sigma_p(R)$ profiles (the smoothing procedure is described in Churazov et al. 2010). The profiles $I(R)$ and $\sigma_p(R)$ for M87 are shown in Figure 2, panels (A) and (B). The stellar surface density from Kormendy et al. (2009) is shown as red squares. The velocity dispersion measurements from SAURON and VIRUS-P are shown as red circles and black squares, respectively. When smoothing the projected velocity dispersion profile, we use only SAURON data in the radial range $R \lesssim 8''$, both SAURON and VIRUS-P between $8'' \leq R \leq 16''$ and only VIRUS-P for $R \geq 16''$ as is done in M11. The logarithmic derivatives are shown in panel (C). Note that $\alpha \approx 2$ in the range $100'' \leq R \leq 300''$. In this radial range we expect a weak dependence on the anisotropy parameter β and the isotropic circular velocity curve to be a good representation of the true circular speed profile. Using equations (4) we calculate $V_c(R)$ for an isotropic distribution of stellar orbits (shown in blue), for pure radial and pure circular orbits (in green and magenta, correspondingly). These three curves intersect each other at the sweet spot $R_{\text{sweet}} \approx 141''$ where we estimate $V_c^{\text{opt}}(R_{\text{sweet}}) \equiv V_c^{\text{iso}}(R_{\text{sweet}}) \approx 524.3 \text{ km s}^{-1}$. The relative error of this estimate at R_{sweet} with respect to the circular speed $V_c^M(R_{\text{sweet}})$ from M11 (Figure 2, panel (D), solid black line) is equal to $\Delta = (V_c^{\text{opt}} - V_c^M)/V_c^M = 3.3\%$.

Within expected uncertainties³ our simple estimate at the sweet point agrees well with the circular speed obtained from Schwarzschild modeling.

The method under consideration is not only simple and fast in implementation, the resulting estimate does not strongly depend on the quality of observational data. To demonstrate this we apply the analysis to the set of data used in the state-of-the-art modeling of M87 by Gebhardt and Thomas (2009) (hereafter ‘GT09’). GT09 as well as M11 derive the mass profile of M87 employing basically the same axisymmetric orbit-based dynamical models.

³ 5.4% was found in Lyskova et al. (2012) for a sample of simulated massive slowly rotating simulated galaxies

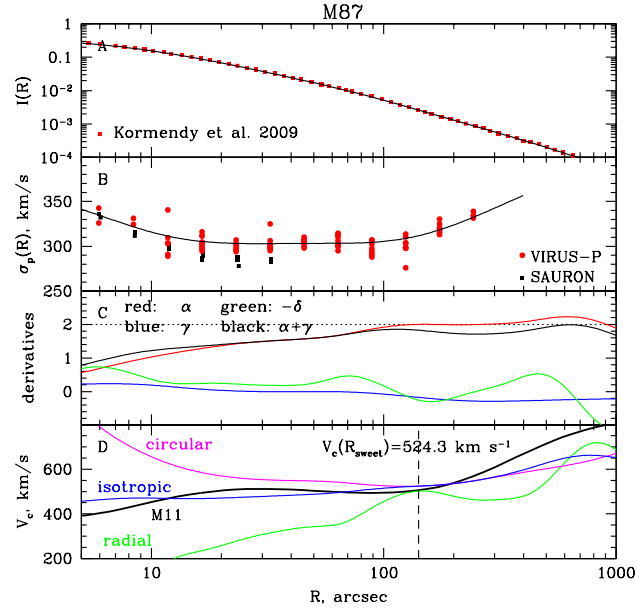


Figure 2. Circular speed estimate of M87. The stellar surface brightness and the line-of-sight velocity dispersion profiles are shown in panels (A) and (B) correspondingly. Data are represented as points and smoothed curves used to compute the auxiliary coefficients α, γ, δ as black solid lines. The logarithmic derivatives $\alpha, \gamma, -\delta$ and $\alpha + \gamma$ (eq. 5) are shown in panel (C) in red, blue, green and black, respectively. Circular velocity curves for isotropic orbits of stars (in blue), pure radial (green) and pure circular (magenta) orbits as well as the circular speed (in black) derived in M11 are presented in panel (D).

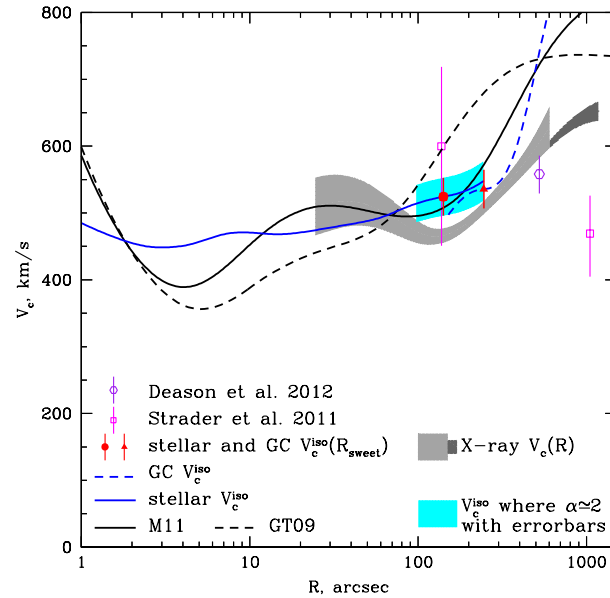


Figure 3. Comparison of the simple circular speed estimates for M87 with V_c -profiles inferred from the state-of-the-art modeling. The solid line shows the best-fitting model of M11, the dashed line - the V_c -profile from GT09. V_c^{iso} resulting from the same set of data (mainly, stellar kinematic and photometry) as used in M11 is shown as a blue solid line. The dashed blue line is V_c^{iso} -profile derived from GC data as used in GT09. The red circle and the red triangle represent our simple V_c -estimates derived on the basis of same data sets used in M11 and in GT09, respectively. Shown in grey are X-ray V_c -profiles from Chandra and XMM data with errorbars. V_c -estimates from recent works (Deason et al. 2012 and Strader et al. 2011) are shown as purple and magenta dots with errorbars.

The only difference is the observational data used. GT09 use stellar kinematic data from SAURON (Emsellem et al. 2004) and from van der Marel (1994) at $R \lesssim 40''$. At larger radii GT09 use the surface density profile from McLaughlin (1999) for the globular clusters (GC) and individual globular cluster velocities reported in Côté et al. (2001). For this data set our analysis results in $V_c = 535.6 \text{ km s}^{-1}$ at $R_{\text{sweet}} = 245.5''$. This estimate is basically based only on the GC data. It is about 21% smaller than the circular speed derived by GT09 but it agrees well ($\Delta = 6.4\%$) with the rotation curve from M11. Figure 3 shows the circular speed profiles resulting from different methods. The profiles derived from detailed dynamical modeling of M11 and GT09 are shown as black solid and dashed lines, respectively. The simple V_c -estimates derived in this work are shown as a red circle (based on the set of data used in M11) and a red triangle (from data used in GT09). V_c^{iso} in the radial range where the log-slope of the surface brightness $\alpha \simeq 2$ with expected uncertainties ($\pm 5.4\%$) is shown in cyan. The grey shaded region represents the result of the X-ray analysis of available archive XMM and Chandra data. The X-ray data are deprojected assuming spherical symmetry to derive gas density and temperature profiles (see Section 3.3.1 for more detail). Using derived profiles and the hydrostatic equilibrium equation the mass profile is derived. The width of the shaded area is determined mainly by systematic deviations of $V_c(R)$ derived under an assumption of a fixed or free metal abundances (see details in Section 3.3.1) rather than statistical variations. The dark grey shaded region is based on XMM data only. The discrepancy between the profiles from dynamical modeling and from X-ray analysis can be explained by the contribution of a gas non-thermal pressure to the total pressure (Churazov et al. 2008). A wiggle in the X-ray-based $V_c(R)$ at $R \sim 200''$ is due to a quasi spherical shock generated by the supermassive black hole at the center of M87.

If we compare the optical circular speed estimate for M87 at the sweet spot with the X-ray based one at the same radius, we get $\frac{V_c^{\text{opt}}}{V_c^{\text{X}}} \approx 1.12$, what implies $\sim 25\%$ non-thermal pressure support. It should be noted, however, that the sweet radius happens to lie in the vicinity of the shock front (Forman et al. 2007) and the X-ray circular speed might be underestimated in the region of a ‘dip’. Previously, the comparison of the X-ray data on M87 with the analysis of the optical data in Romanowsky and Kochanek (2001) and GT09 has been done in Churazov et al. (2008) and Churazov et al. (2010) respectively. In the first case (Romanowsky and Kochanek 2001 + X-Rays) no evidence for non-thermal pressure in excess of $\sim 10\%$ of the thermal pressure was found, while the comparison with GT09 results yielded a large non-thermal component of order 50%. This discrepancy can be traced to the difference in the optical data. With new data and analysis of M11 this discrepancy largely goes away. Note also, that in Churazov et al. (2008, 2010) the circular speed estimate $\sim 440 \text{ km s}^{-1}$ was derived from X-rays via fitting the gravitational potential by $\Phi(R) = V_c^2 \ln r + \text{const}$ in the broad radial range from $0.1'$ to $5'$.

3.2 Observations and data reduction

The spectroscopic observations at the prime focus of the SAO RAS 6-m telescope were made with the multi-mode focal reducer SCORPIO (Afanasiev and Moiseev 2005) and its new version SCORPIO-2 (Afanasiev and Moiseev 2011). When operated in the long-slit mode, both devices have same slit 6 arcmin in height with a scale of 0.36 arcsec per pixel. However, with a similar spectral resolution SCORPIO-2 provides twice larger spectral range. The CCDs employed were an EEV 42-40 in the SCORPIO and E2V 42-90 in the SCORPIO-2.

Table 1 lists the target galaxies and Table 2 gives the log of observations: the position angles of the spectrograph slit for each galaxy, the observing date, the slit width, spectral range, spectral resolution (estimated by the mean FWHM of air glow lines), total exposure T_{exp} , and seeing. Usually we observed targets with two slit positions: along photometric major and minor axes. The exceptions are NGC 708 (the second slit was placed along the dust lane crossed galaxy nucleus) and UGC 3957 where observations only along major axis have been performed.

The data reduction were made in a standard way using the IDL-based software package developed at the SAO RAS (Afanasiev and Moiseev 2005). The measurements of the distribution of line-of-sight velocities V_{rot} and stellar velocity dispersion σ_p were carried out by cross-correlating the spectra of galaxies with the spectra of the template star observed on the same nights. The measurement technique has already been described in our previous papers (Moiseev 2001; Sil'chenko, Moiseev A. V. and Shulga 2010). We observed several template stars belonging to the spectral types III G8 - III K5 and also twilling light sky (i.e. solar spectrum). For the final measurements, we selected a template giving a maximum correlation coefficient. During the stellar kinematics parameters estimation we applied logarithmic binning along the slit to provide a sufficient signal-to-noise ratio ($S/N > 15 - 20$ per bin in each pixel). Also in each beam we calculated the surface brightness $I(R)$ as an integral intensity of stellar continuum at the range $5040 - 5140 \text{ \AA}$. The Figure 4 shows the results of our spectral observations together with V-band images of the galaxies taken at the same nights in the direct image mode of SCORPIO and SCORPIO-2.

3.3 Rotation Curves

3.3.1 Circular speed from X-ray data.

Using publicly available Chandra data we have derived the circular speed profiles for galaxies in our sample under the assumption of the hydrostatic equilibrium. We follow the procedure of the data analysis described in Churazov et al. (2010). Here we only outline the major steps.

First, in each observation we follow the reduction procedure described in Vikhlinin et al. (2005), i.e. filter out high background periods and apply the latest calibration corrections to the detected X-ray photons, and determine the background intensity.

As a next step we apply a non-parametric deprojec-

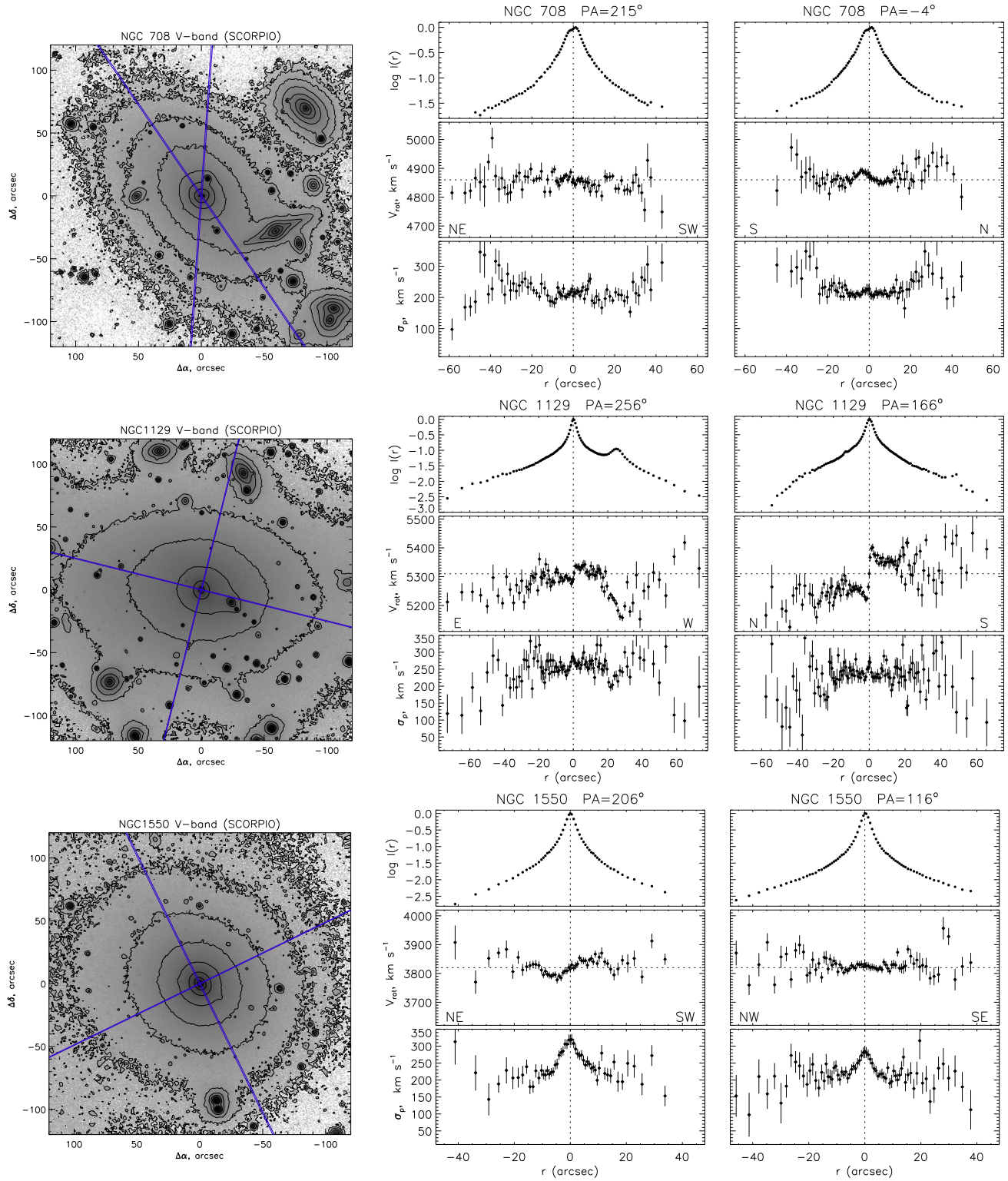


Figure 4. The results of the SAO RAS 6-m telescope observations. Left: V-band image in logarithmic grey-scale and positions of the spectrograph slits. Middle: the distributions of stellar continuum surface brightness, line-of-sight velocities and velocity dispersion of stars along major axis. The dotted lines mark the position of nucleus and accepted systemic velocity. In the case of NGC 1129 at $r \approx 20 - 30$ arcsec the slit crosses the companion galaxy. Right: the same for the second slit position. At large radii velocity dispersion uncertainties are likely underestimated as they do not account for systematic errors coming from the sky subtraction.

Table 1. Sample of elliptical galaxies. The columns are: (1) - common name of the galaxy; (2) - redshift from the NASA/IPAC Extragalactic Database; (3) - adopted distance; (4) - central velocity dispersion from HyperLeda; (5) - hydrogen column density from (Dickey and Lockman 1990).

Name (1)	z (2)	D , Mpc (3)	σ_c , km s $^{-1}$ (4)	N_H , 10^{20} cm $^{-2}$ (5)
NGC 708	0.016195	68.3	229.8 ± 9.7	5.37
NGC 1129	0.017325	73.1	329.5 ± 15.1	9.81
NGC 1550	0.012389	52.1	308.0 ± 6.2	11.5
NGC 4125	0.004523	23.9	226.8 ± 6.9	1.84
UGC 3957	0.034120	145.9	331.1 ± 35.1	4.63

Table 2. Log of the observations

Galaxy	Slit PA (deg)	Date	Slit width (arcsec)	Sp. range (Å)	Sp. resol. (Å)	Exp. time (min)	Seeing (arcsec)
NGC 708	-4	05.10.2011	1.0	4840–5610	2.2	180	1.1–1.2
	215	03.10.2011	1.0	4840–5610	2.2	185	1.4–3.5
NGC 1129	166	21.10.2012	0.5	4080–5810	3.0	180	1.2–1.4
	256	15.10.2012	0.5	4080–5810	3.0	180	1.4–1.5
NGC 1550	116	09.12.2012	1.0	3700–7200	5.1	180	1.5–1.6
	206	16-17.10.2012	0.5	4080–5810	3.0	180	1.3–1.6
NGC 4125	175	14.04.2013	1.0	4840–5610	2.2	160	1.2–1.3
	265	19.10.2012	0.5	4080–5810	3.0	200	1.6–1.7
UGC 3957	287	03.11.2010	1.0	4415–6015	2.2	180	1.1–1.5

tion procedure described in Churazov et al. (2003, 2008). In brief, the observed X-ray spectra in concentric annuli are modeled as a linear combination of spectra in spherical shells; the two sequences of spectra are related by a matrix describing the projection of the shells into annuli. To account for the projected contribution of the emission from the gas at large distances from the center (i.e., at distances larger than the radial size r_{max} of the region well covered by actual observations) one has to make an explicit assumption about the gas density/temperature profile. We assume that at all energies the gas volume emissivity at $r > r_{max}$ declines as a power law with radius. The slope of this power law is estimated based on the observed surface brightness profile at $r \lesssim r_{max}$. Since we assume that the same power law shape is applicable to all energy bands, effectively this assumption implies constant spectral shape and therefore the isothermality of the gas outside r_{max} . The contribution of these layers is added to the projection matrix with the normalization as an additional free parameter. The final projection matrix is inverted and the shells' spectra are explicitly calculated by applying this inverted matrix to the data in narrow energy channels.

The resulting spectra are approximated in XSPEC (Arnaud 1996) with the Astrophysical Plasma Emission Code (APEC) one-temperature optically thin plasma emission model (Smith et al. 2001). The redshift z (from the NASA/IPAC Extragalactic Database – NED) and the line-of-sight column density of neutral hydrogen N_H (Dickey and Lockman 1990) have been fixed at the values given in Table 1. For each shell we determine the emission measure (and therefore gas density) and the gas tempera-

ture. These quantities are needed to evaluate the mass profile through the hydrostatic equilibrium equation. For cool (sub-keV) temperatures and approximately solar abundance of heavy elements, line emission provides a substantial fraction of the 0.5–2 keV flux. With spectral resolution of current X-ray missions the contributions of continuum and lines are difficult to disentangle. As a result the emission measure and abundance are anti-correlated, which can lead to a large scatter in the best-fit emission measures. As an interim (not entirely satisfactory) solution, we fix the abundance at 0.5 solar for all shells, using the default XSPEC abundance table of Anders & Grevesse (1989). We return to this issue below.

Knowledge of the gas number density n and temperature T in each shell allows us to evaluate the $M(R)$ or $V_c(R)$ profile by using the hydrostatic equilibrium equation:

$$-\frac{1}{\rho} \frac{dP}{dr} = \frac{d\Phi}{dr} = \frac{V_c^2}{r} = \frac{GM}{r^2}, \quad (8)$$

where $P = nkT$ is the gas pressure, $\rho = \mu m_p n$ is the gas density (m_p is the proton mass). The mean atomic weight μ is assumed to be equal to 0.61.

The resulting circular speed profiles $V_c^X(r)$ for all galaxies in our sample are shown as black thick lines with error bars represented as black shaded regions in lower panels of Figure 6. One should keep in mind that in assuming hydrostatic equilibrium one neglects possible non-thermal contribution to the pressure, arising from turbulence in the thermal gas, cosmic rays, magnetic fields and non-radiating relativistic protons (e.g., Churazov et al. 2008). So comparing optical and X-ray estimates of the circular speed may provide constraints on the contribution of the non-thermal

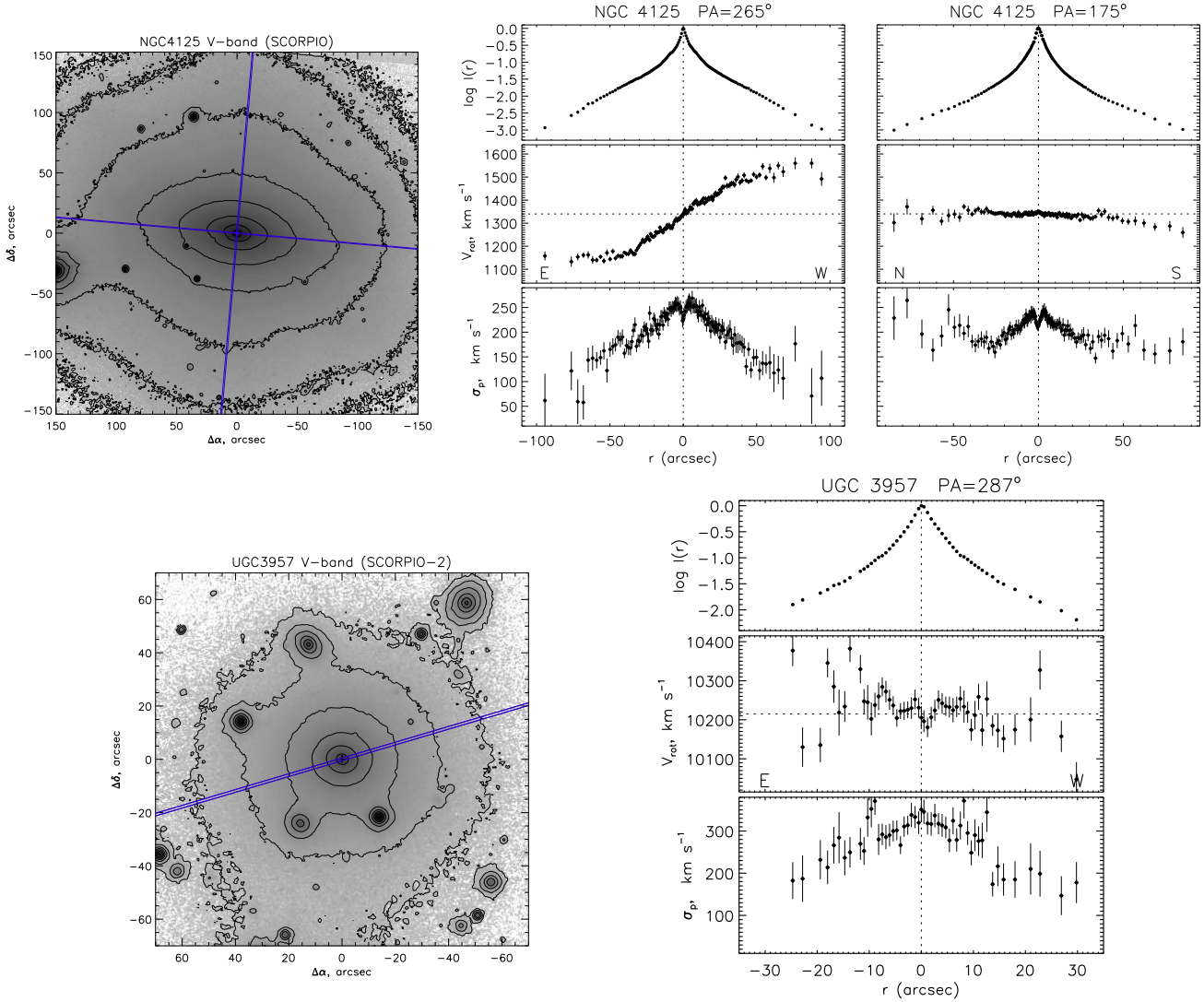


Figure 4. (continue)

particles to the gas pressure. High-resolution cosmological simulations of galaxy clusters suggest that the gas motions contribute $\sim 5\%$ of the total pressure support at the center and up to $\sim 15 - 20\%$ at r_{500} in relaxed systems (e.g. Lau, Kravtsov, Nagai 2009; Zhuravleva et al. 2013). Recent studies on combining X-ray mass measurements and sophisticated stellar dynamical methods imply up to $\sim 50\%$ non-thermal support (e.g. Shen and Gebhardt 2010, Rusli et al. 2011, GT09), although the uncertainties in model assumptions may be significant (Buote and Humphrey 2012). As our simple method provides a mass-estimate that is robust and largely insensitive to the orbital anisotropy at the sweet point, we interpret the offset at R_{sweet} between the X-ray and optical measurements as a signature of deviations from hydrostatic equilibrium. In particular, the ratio $f_{nt} = (M_{opt} - M^X)/M_{opt}$ provides an estimate of the fractional contribution of the nonthermal pressure to the total pressure, provided that this fraction does not vary with ra-

dius. In this approximation $M^{X,c}(r) = M^X(r)/(1 - f_{nt})$ is an estimate of the mass at other radii.

As the gas pressure is assumed to be isotropic, mismatch between the corrected X-ray circular speed $V_c^{X,c}$ and the isotropic one V_c^{iso} derived from the Jeans equation may give a clue regarding the orbital structure of the galaxy. E.g., at small radii $V_c^{X,c} > V_c^{iso}$ would suggest more circular orbits, while at larger radii this would correspond to more radial orbits. Of course, the reliability of such analogy strongly depends on the derived V_c^X and V_c^{iso} .

We now illustrate the impact of our assumption of a flat abundance profile $Z = 0.5Z_{\odot}$ and estimate arising errors on the inferred circular speed.

At low temperatures ($\lesssim 2$ keV) metal abundances derived from X-ray spectra with the limited energy resolution of current X-ray missions suffer from the ambiguity of disentangling line emission and continuum. While derived circular velocity is weakly sensitive to the particular value of

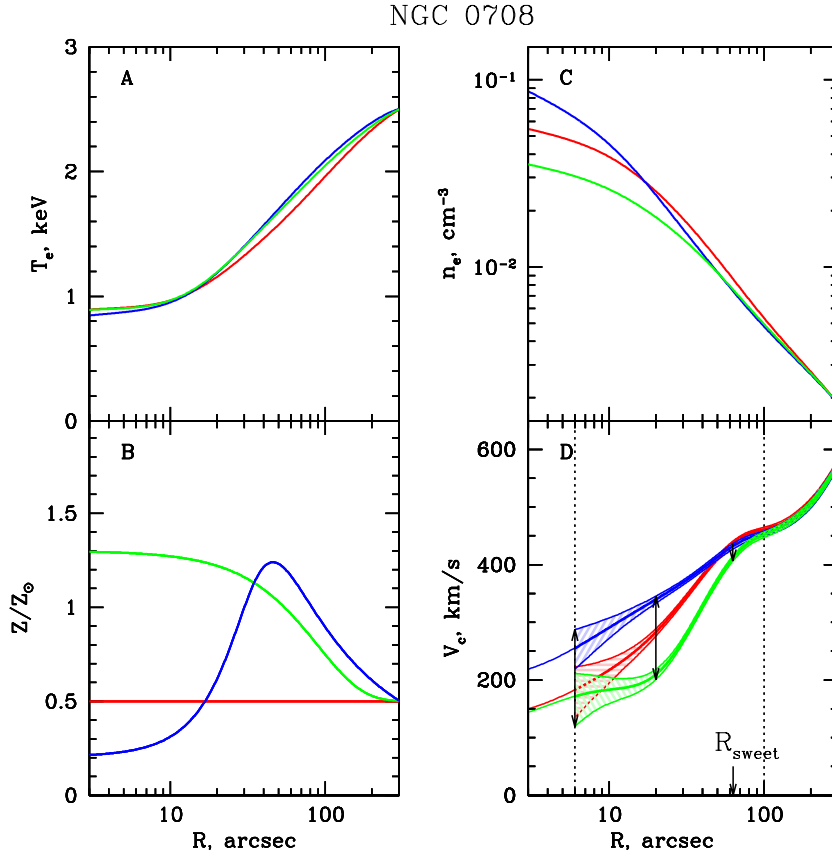


Figure 5. The effect of the abundance gradient on the calculated circular speed profile. Panel (A) shows the deprojected temperature for NGC 0708, panel (B) - assumed models for the metallicity, panel (C) - gas density profiles and panel (D) - resulting circular velocity curves with 1σ errors from 1000 Monte Carlo realizations. The vertical dotted lines indicate a region of interest where both optical and X-ray data are available. The arrows show the spread in circular speed estimates coming from different abundance profiles.

metallicity in the spectral models, it can be significantly affected by the radial variations of the heavy-element abundance (e.g. Johnson et al. 2009; Churazov et al. 2010).

Since abundance measurements can be biased (e.g. Buote 2000) we tried to make a conservative estimate of the varying abundance profile impact by setting by hand several model metallicity profiles and fitting the deprojected data again, leaving the normalization and temperature as free parameters⁴.

As an example, we show in Figure 5 the derived density, temperature and circular speed profiles⁵ for NGC 0708. The estimated statistical errorbars come from 1000 Monte Carlo simulations. Here we consider 3 models: (i) flat abundance profile $Z = 0.5Z_\odot$ (shown in red), (ii) fit to the de-

projected abundance with a ‘dip’ at the center (in blue) and (iii) physically motivated model (in green), where the metal abundance rises to the galaxy center as is generally expected for elliptical galaxies (e.g. Humphrey and Buote 2006). Compared to the flat abundance profile, the metallicity monotonically increasing towards the center leads to the flattening of the gas density profile and lowering the final circular speed estimate. In contrast, the decreasing to the center $Z(r)$ ‘boosts’ inferred V_c^X , as is clearly seen from Figure 5.

Other galaxies in our sample show only monotonical increase of the deprojected metal abundance to the center, so the spread in final V_c^X -estimates is smaller. The circular velocity profiles corresponding to the flat abundance (thick solid black lines) and 1σ -errors from 1000 Monte Carlo simulations (black shaded area enclosed by two thin black lines) are shown in Figure 6.

3.3.2 Optical Rotation Curves

All observed galaxies in the sample are quite massive, close to spherical and slowly rotating (except maybe NGC 4125).

⁴ One may consider the stellar metallicity profiles from the absorption indices (Section 3.3.4) as input $Z(r)$. For our sample galaxies this assumption does not affect the final estimates in a significant way.

⁵ As eq. (8) requires differentiation, to calculate derivatives we smooth density, temperature and pressure profiles following the procedure described in Churazov et al. (2010). The typical value of the smoothing width is ~ 0.55 .

This makes them suitable for our analysis. According to the algorithm for estimating the circular speed described in Section 2.2 we perform the following steps:

(i) First, given the surface brightness I_i , projected velocity dispersion σ_{pi} with its errors $\Sigma_{\sigma i}$ and rotational velocity $V_{rot i}$ with its errors $\Sigma_{rot i}$ along two slits ($i = 1, 2$) we construct the average profiles

$$I = \frac{I_1 + I_2}{2}; \quad (9)$$

$$\sigma_p^2 = \frac{I_1 \sigma_{p1}^2 / \Sigma_{\sigma 1}^2 + I_2 \sigma_{p2}^2 / \Sigma_{\sigma 2}^2}{I_1 / \Sigma_{\sigma 1}^2 + I_2 / \Sigma_{\sigma 2}^2}. \quad (10)$$

If rotation velocity along the slit $V_{rot i}$ is not negligible, then instead of σ_p we use V_{rms} defined as

$$V_{rms}^2 = \frac{I_1 V_{rms1}^2 / \Sigma_{rms1}^2 + I_2 V_{rms2}^2 / \Sigma_{rms2}^2}{I_1 / \Sigma_{rms1}^2 + I_2 / \Sigma_{rms2}^2}, \quad (11)$$

where $\Sigma_{rms i}^2 = \Sigma_{\sigma i}^2 + \Sigma_{rot i}^2$; $\Sigma_{rot i}$ are the errorbars assigned to rotation velocity measurements.

(ii) Then we calculate the logarithmic derivatives α , γ and δ from the derived profiles using equations (5).

(iii) Next, we compute the circular speed $V_c(R)$ for isotropic, radial and circular stellar orbits using equations (4) in case of reliable data (full analysis) or equations (6) in case noisy or systematics affected observational line-of-sight velocity dispersion profile (simplified analysis). As discussed above, for rotating galaxies one should use $V_{rms}(R)$ instead of $\sigma_p(R)$ in equations (4) or (6).

(iv) $V_c^{iso}(R_{sweet})$ is taken as a final estimate of V_c at the sweet spot R_{sweet} - the radius at which all three curves $V_c^{iso}(R)$, $V_c^{circ}(R)$ and $V_c^{rad}(R)$ are maximally close to each other. At R_{sweet} the sensitivity of the method to the anisotropy parameter β is expected to be minimal so the estimation of the circular speed at this particular point is not affected much by the unknown distribution of stellar orbits. In case of the simplified version of the analysis $R_{sweet} \equiv R_2$, where $\alpha = -\frac{d \ln I(R)}{d \ln R} = 2$.

(v) Finally, we compare derived V_c -estimates with the X-ray circular speed at the same radius. Table 3 summarizes the results, providing both optical and X-ray circular speed estimates as well as the temperature of the hot gas at R_{sweet} . The scatter in optical V_c arises from differences in observed $I(R)$ and $\sigma_p(R)$ along two slits or from measurement errors of $\sigma_p(R)$ when information is available along one slit only. Errors for X-ray derived V_c comes from 1000 Monte Carlo realizations. In parentheses we present the conservative estimate of errors for the case of radially varying metallicity.

In Figure 6 we present results of the analysis. The logarithmic slope of the surface brightness profile for each galaxy in our sample is shown in panel A. Thin red lines correspond to slopes measured along the individual slits, while the thick lines show the average profiles (eq. 9). The shaded area indicates the scatter in profiles arising from different slits (when available). The derived profiles for V_c^{iso} , V_c^{circ} and V_c^{rad} are shown in panel B in blue, magenta and green correspondingly. Again, the thin lines represent the V_c -curves resulting from measurements along each individual slit, while

the thick lines demonstrate the average profiles coming from equations (9)-(11). If information is available along two slits, then the shaded regions (paleblue for V_c^{iso} , plum for V_c^{circ} and palegreen for V_c^{rad}) show the scatter between these slits, in a case when profiles are measured along one slit only, the shaded regions indicate the measurements errors of $\sigma_p(R)$. The circular speed profiles derived from Chandra data are overplotted with errorbars in black. Stellar contribution to the circular velocity derived for the Salpeter and Kroupa IMF is shown in yellow (see Section 3.3.4).

3.3.3 Comments on individual galaxies.

• NGC0708

NGC 0708 (Figure 6, upper left corner) is a cD galaxy located at the center of Abell 262 galaxy cluster. The surface brightness and the projected velocity dispersion profiles are available for two slit positions oriented at P.A. = -4° and at P.A. = 215° . The surface brightness profile along the slit at P.A. = -4° declines very slowly, the logarithmic slope $\alpha = -d \ln I(R)/d \ln R$ does not exceed 1.5 in observed range of radii leading to a diverging total stellar mass. Such a behaviour may be a result of influence of cluster gravitational potential. So for our analysis we use information along the slit at P.A. = 215° only. The projected velocity dispersion is close to being flat at $R \lesssim 30''$ and gets systematics affected at larger radii. So we use the simplified version of the analysis. Results of our analysis are presented in the upper left corner of Figure 6. The surface brightness slope (for the slit at P.A. = 215°) is shown in panel A, derived circular velocity profiles different types of orbits are plotted in panel B. The shaded areas indicate uncertainties in derived V_c^{iso} (paleblue), V_c^{circ} (plum) and V_c^{rad} (palegreen), coming from measurement errors of $\sigma_p(R)$. The sweet radius where the sensitivity of the method to the anisotropy is minimal is located at $63''$, i.e slightly beyond the range of radii where optical data are available. Although the reliability of such the estimate is unclear the extrapolated V_c^{iso} lies quiet close to the circular speed curve derived from X-ray analysis.

• NGC1129

NGC 1129 is a giant elliptical galaxy located in the center of a poor cluster AWM 7. In Figure 6 (upper right) are shown results of optical and X-ray analyses. Before estimating the circular speed from optical data we have excluded regions where the surface brightness profile seems to be contaminated by projection of companions. The exclusion is done on the basis of visual inspection. So we consider the surface brightness profile along the slit positioned at P.A. = 166° in radial range from $-55''$ till $41''$ and in case of P.A. = 256° slit - at $R \leq 0''$. The projected velocity dispersion profile looks nearly flat at $R \lesssim 20''$ and is getting noisy at $R \gtrsim 20''$, so we assume $\sigma_p(R) \equiv const = 257 \text{ km s}^{-1}$ (the surface brightness weighted average value). Optical V_c^{iso} -estimate in the sweet region (which is coincident with a range of radii where $\alpha \approx 2$) is consistent with the circular speed derived from hydrostatic equilibrium of hot gas in the galaxy. Moreover, V_c^{iso} and V_c^X agree within errorbars over the range of radii where both optical and X-ray data are available. It

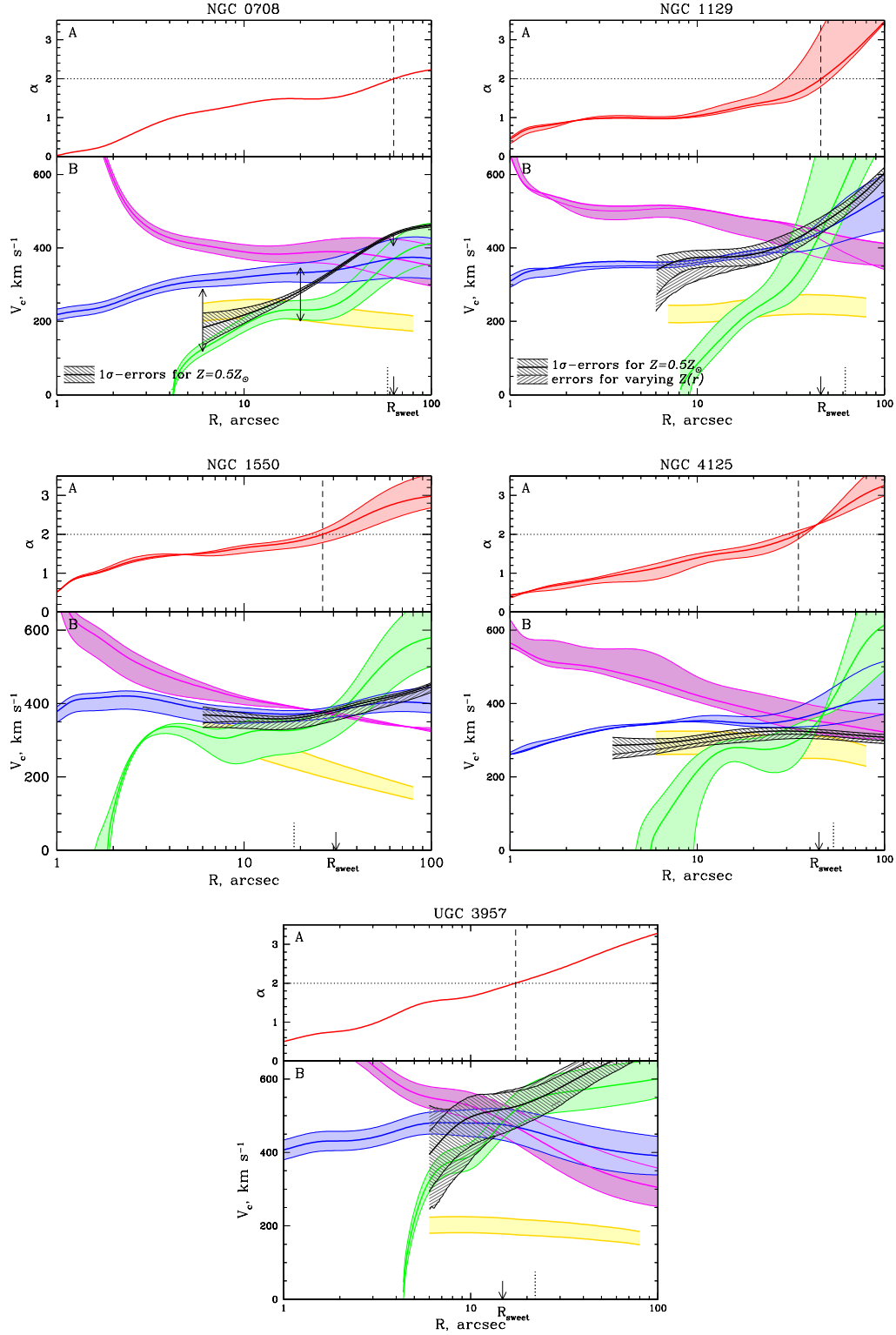


Figure 6. Panel A - the surface brightness logarithmic slope α (red curve) and location of R_2 where $\alpha = 2$ (vertical dashed line). Panel B - V_c -profiles for isotropic (blue lines and paleblue shaded area), pure radial (green lines and palegreen shaded area) and pure circular (magenta lines and plum shaded area) orbits. The $V_c(r)$ derived from Chandra data under the assumption of hydrostatic equilibrium is shown as the black thick line. The shaded area shows statistical errorbars for the flat and varying with radius metallicity. For NGC 708 arrows are the same as in Figure 5 and indicate the conservative lower and upper limits on X-ray based $V_c(r)$ coming from radial variations of metal abundance. The stellar contribution to the circular speed profile is presented in yellow (see Section 3.3.4). Location of $R_{\text{eff}}^{\text{slit}}$ defined from the de Vaucouleurs fit to the long-slit surface brightness profile is marked with the dotted line.

Table 3. V_c -estimates for our sample of elliptical galaxies derived from optical and X-ray analyses. The columns are: (1) - common name of the galaxy; (2) - sweet radius; (3) - optical V_c -estimate at R_{sweet} ; (4) - V_c -estimate at R_{sweet} from X-ray, in parentheses are presented the conservative error estimates; (5) - gas temperature at R_{sweet} .

Name (1)	R_{sweet} , arcsec (2)	V_c^{iso} , km s $^{-1}$ (3)	V_c^X , km s $^{-1}$ (4)	kT, keV (5)
NGC 708	63.1	371^{+53}_{-53}	437^{+4}_{-4} (-31)	1.7
NGC 1129	45.7	444^{+31}_{-44}	464^{+20}_{-25}	3.0
NGC 1550	30.9	382^{+12}_{-19}	383^{+5}_{-6} (-29)	1.2
NGC 4125	44.7	375^{+45}_{-36}	322^{+7}_{-9} (-18)	0.5
UGC 3957	14.8	476^{+43}_{-43}	518^{+45}_{-66} (+47)	2.2

should be noted that NGC1129 shows significant minor axis rotation, indicating a triaxial intrinsic shape of the galaxy.

- NGC1550

NGC 1550 is a S0 galaxy lying at the center of a luminous galaxy group. The surface brightness and the projected velocity dispersion profiles are available for two slit positions oriented at P.A. = 116° and at P.A. = 206°. Rotation velocity is consistent with zero. The profiles do not have any peculiar features so we use all available information to estimate the circular speed. The results of our analysis are shown in Figure 6, left side of a middle panel. Note that the circular velocity corresponding to the isotropic distribution of stellar orbits is nearly constant over the whole available range of radii and it coincides within errorbars with the X-ray circular speed profile. This fact could indicate that the gravitational potential of NGC 1550 is close to isothermal and the galaxy is dynamically relaxed with hot gas being in hydrostatic equilibrium.

- NGC4125

NGC4125 (Figure 6, middle right side) is a E6 galaxy located at the center of NGC 4125 group of galaxies. It is the only galaxy in our sample with significant rotation. To take the rotation into account we use $V_{\text{rms}}(R) = \sqrt{\sigma_p(R)^2 + V_{\text{rot}}(R)^2}$ instead of $\sigma_p(R)$ in equations (4). The isotropic circular speed V_c^{iso} slightly exceeds V_c^X over the whole range of radii where the optical observations are available what may indicate the the non-thermal pressure support at the level of $f_{nt} \approx 36\%$ at the sweet point.

- UGC3957

UGC3957 (Figure 6, lower panel) is an elliptical galaxy at the center of UGC 03957 group. It has been observed using only one slit positioned at P.A. = 287°. As in case with NGC 0708 shaded areas indicate uncertainties in derived V_c -profiles, arising from measurement errors of $\sigma_p(R)$. At the sweet point V_c -estimate from optical data agrees with X-ray derived one. The discrepancy between optical $V_c(R)$ and X-ray $V_c^X(R)$ may indicate that at $r \gtrsim 20''$ anisotropy parameter $\beta > 0$ if the hydrostatic equilibrium approximation is valid.

3.3.4 Stellar populations: properties, mass-to-light ratios, contributions to the total mass

By using the same SCORPIO/BTA long-slit spectral data, we have calculated Lick indices $H\beta$, Mgb , $Fe5270$, and $Fe5335$ along the slit, to derive the ages and chemical abundances which are in turn used to estimate mass-to-light ratios of the stellar component varying along the radius and to calculate properly the mass contributed by the stellar component within the radius R_{sweet} . Our approach to the Lick index calibrations can be found in Baes et al. (2007).

Our spectral data are rather deep and have provided the profiles of high-precision Lick indices up to 1.1 – 2.2 effective radii from the center in four galaxies of five. Figure 7 presents the comparison of the major-axis Lick index profiles in NGC 4125 according to our measurements with those by Pu et al. (2010) obtained at the 9.2m Hobby-Eberly telescope. The agreement is rather good, and the index point-to-point scatters are comparable. Figure 8 compares our data for NGC 708 with the data from Wegner et al. (2012) at two slit positions (we don't compare $H\beta$ measurements near the center because we have not been able to correct them properly for the emission contamination). This time our data are much more precise, and the Lick index profiles are much more extended than the data by Wegner et al. (2012) obtained at the 2.4m Hiltner Telescope.

We have confronted our Lick index measurements along the radii in the galaxies under consideration to the Simple Stellar Population (SSP) models by Thomas et al. (2003) which allow to vary magnesium-to-iron ratio. Indeed, giant elliptical galaxies are known to be magnesium-overabundant (Trager et al. 2000) so it must be taken into account when age diagnostics are applied. By confronting $\langle Fe \rangle \equiv (Fe5270 + Fe5335)/2$ vs Mgb , we have found that indeed in four galaxies $[Mg/Fe] = +0.3$ being constant along the radius, while only in NGC 4125 $[Mg/Fe] = +0.1$ with slightly different behaviour along the major and the minor axes: in the latter cross-section, at large radii the $[Mg/Fe]$ comes to +0.3 (Figure 10). This difference, together with the fast rotation along the major axis, gives an evidence for an embedded stellar disc in NGC 4125; so we would prefer to give more weight to the stellar mass-to-light ratio profile along the minor axis (see below). The estimates of the SSP-equivalent (mean, star luminosity-weighted) ages made by confronting the $H\beta$ index to the complex metal-line index $[MgFe]$ (Figure 9) indi-

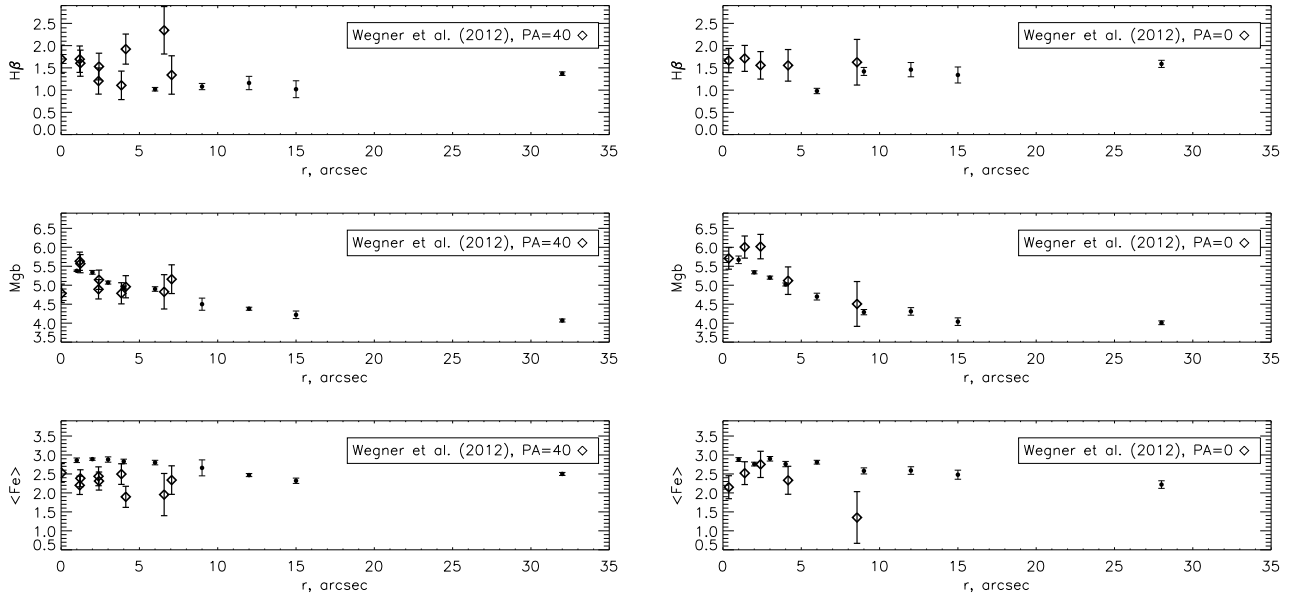


Figure 8. The comparison of the Lick index profiles in NGC 708, according to our data and to the data by Wegner et al. (2012), in two slit orientation.

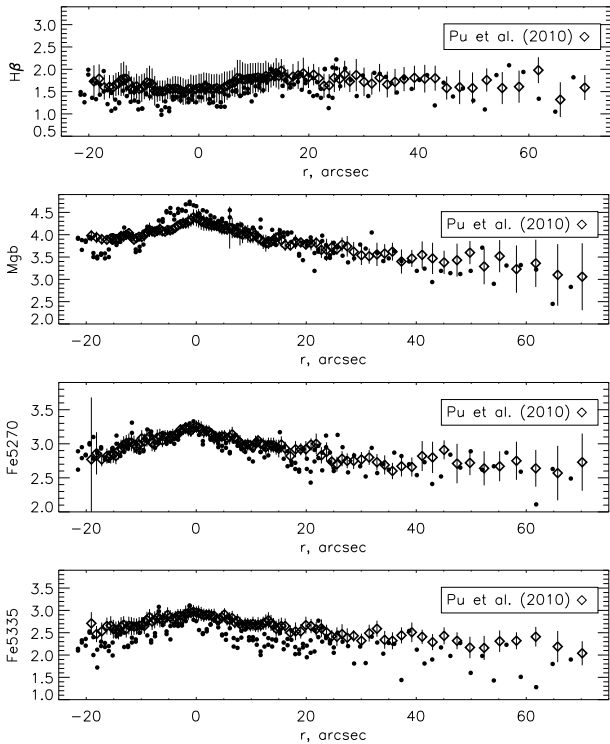


Figure 7. The comparison of the Lick index profiles along the major axis in NGC 4125, according to our data and to the data by Pu et al. (2010).

cate mostly old stellar population, older than 8 Gyr, beyond the very centers of the galaxies; however the stellar nuclei of UGC 3957, NGC 1129, and NGC 1550 may be as young as

5 Gyr old (in NGC 708 we cannot estimate the age of the nuclear stellar population because of the very strong gaseous emission contaminating the $H\beta$ index).

Figure 10 presents in particular the metallicity radial variations in five ellipticals. The metallicity values $[Z/H]$ are plotted against normalized radius, R/R_{eff} , taking into account different values of R_{eff} along the major and the minor axes. The centers of all galaxies demonstrate super-solar metallicity, which is even beyond the model grid of Thomas et al. (2003) in the most massive and luminous galaxy, UGC 3957; however in the outer parts the stellar metallicity drops below the solar value everywhere. The metallicity gradients in our sample ellipticals are negative and can be estimated mostly as from -0.4 to -0.7 dex per dex. In NGC 4125 and NGC 1550 the outer metallicity profiles along the major axis go on above the minor-axis profiles that reveals once more the probable presence of the discs aligned with the major axis, formed in some dissipative events including heavy-element enrichment. We have estimated the metallicity gradients in the spheroids within $0.5R_{\text{eff}}$, $R < 0.5R_{\text{eff}}$, and beyond $0.5R_{\text{eff}}$, $R > 0.5R_{\text{eff}}$ (Table 4), because earlier we have found breaks of the metallicity gradients just near this radius in another sample of elliptical galaxies studied with the long-slit spectroscopy of the SCORPIO/BTA (Baes et al. 2007). Now we have found breaks between steep metallicity gradients in the centers and nearly zero ones in the outer parts at $0.5R_{\text{eff}}$ only in two galaxies having the lower mass – in NGC 0708 and NGC 4125. In massive NGC 1129, NGC 1550, and UGC 3957 the outer metallicity gradients look as steep as the inner ones. Perhaps, for these galaxies we have not reached the radius of break because in the central Coma cluster galaxy NGC 4889 the metallicity gradient break is found at $R = 1.2R_{\text{eff}}$ (Coccatto et al. 2010); perhaps the po-

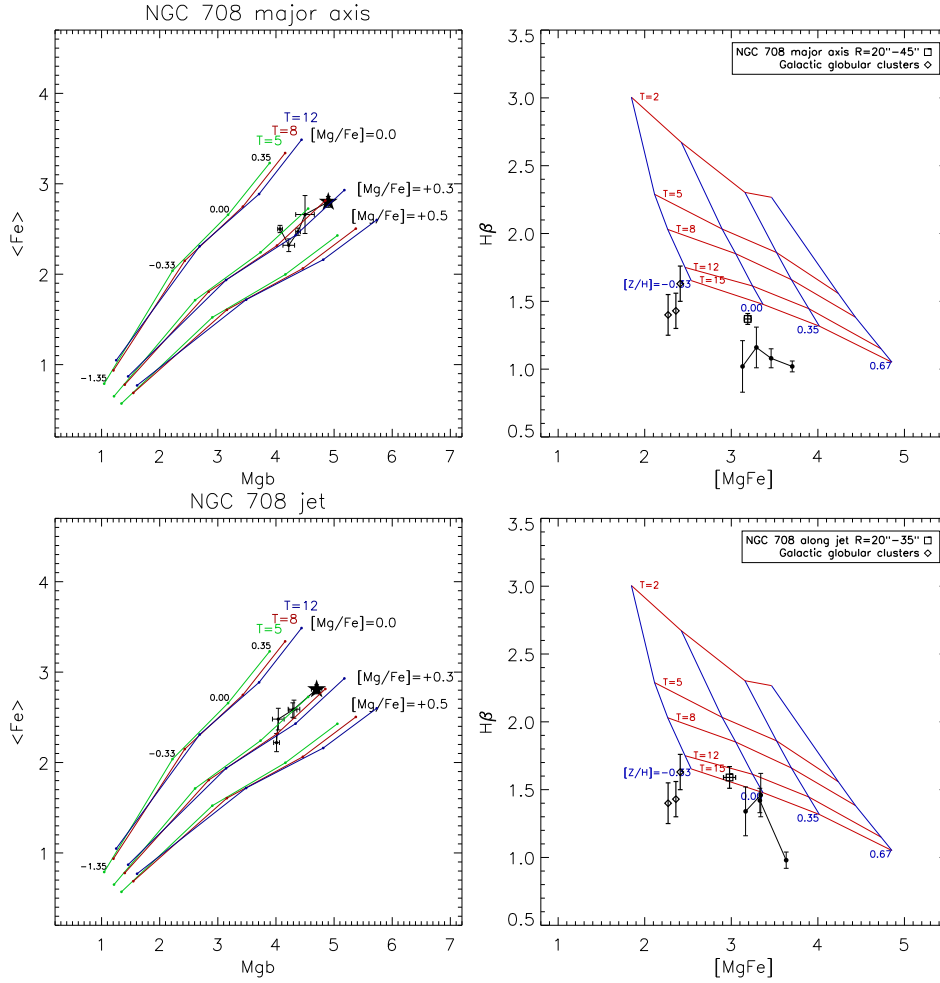


Figure 9. Diagnostic Lick index – index diagrams for all our galaxies in all slit orientations: **(left side)** – The $\langle Fe \rangle$ vs Mgb diagram. The simple stellar population models by Thomas et al. (2003) for three different magnesium-to-iron ratios (0.0, +0.3, and +0.5) and three different ages (5, 8, and 12 Gyr) are plotted as reference. The small signs along the model curves mark the metallicities of +0.35, 0.00, -0.33, and -1.35, if one takes the signs from right to left; **(right side)** – The age-diagnostic diagram for the stellar populations in the central parts of the galaxies under consideration. The stellar population models by Thomas et al. (2003) for $[Mg/Fe] = +0.3$ (for NGC 4125 – for $[Mg/Fe] = +0.0$) and five different ages (2, 5, 8, 12 and 15 Gyr, from top to bottom curves) are plotted as reference frame; the blue lines crossing the model metallicity sequences mark the metallicities of +0.67, +0.35, 0.00, -0.33 from right to left.

Table 4. Metallicity gradient within and beyond the half effective radius.

Galaxy	$\Delta[Z/H]/\Delta \log R$, dex per dex ($R < 0.5R_{\text{eff}}$)	$\Delta[Z/H]/\Delta \log R$, dex per dex ($R > 0.5R_{\text{eff}}$)
NGC 0708 maj. axis	-0.74 ± 0.07	0?
NGC 0708 $PA = -4$	-0.45 ± 0.11	0?
NGC 1129 maj. axis	-0.41 ± 0.07	the same?
NGC 1129 min. axis	-0.50 ± 0.15	the same?
NGC 1550 min. axis	-0.69 ± 0.04	the same?
NGC 4125 min. axis	-0.52 ± 0.05	-0.27 ± 0.18
UGC 3957	–	-2.07 ± 0.33

sition of break radius correlates with the mass of a galaxy. However, the inner metallicity gradients in our galaxies (and the outer one in UGC 3957) are all steeper than -0.3 dex per dex; it means that these inner parts of the elliptical galaxies

under consideration could not be formed by major merger (Kobayashi 2004).

Radial variations of the stellar population mass-to-light ratio in this case reflect mostly the variations of the metallicity. We have calculated $M/L(V)(R)$ in every galaxy by

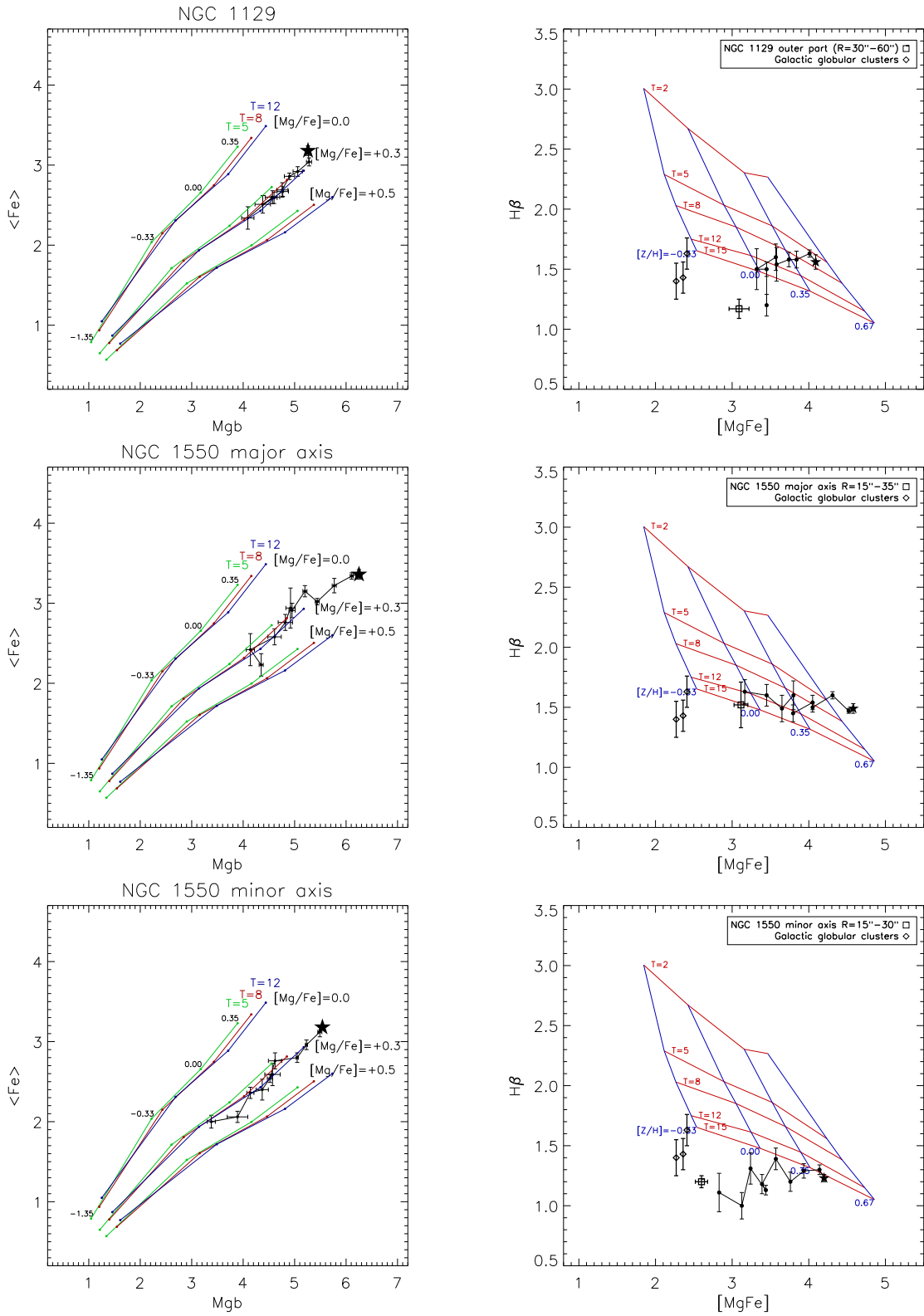


Figure 9. (continue)

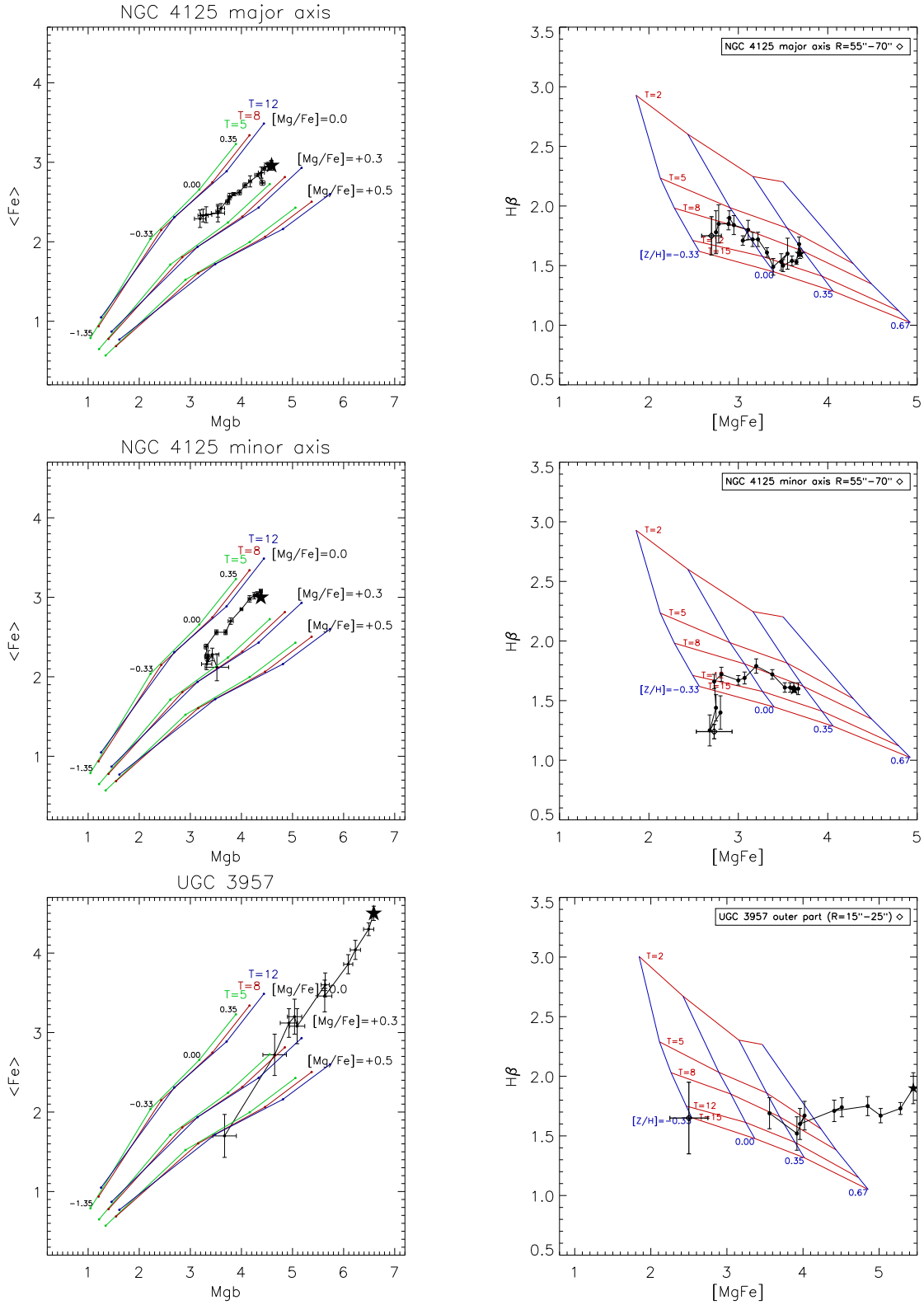


Figure 9. (continue)

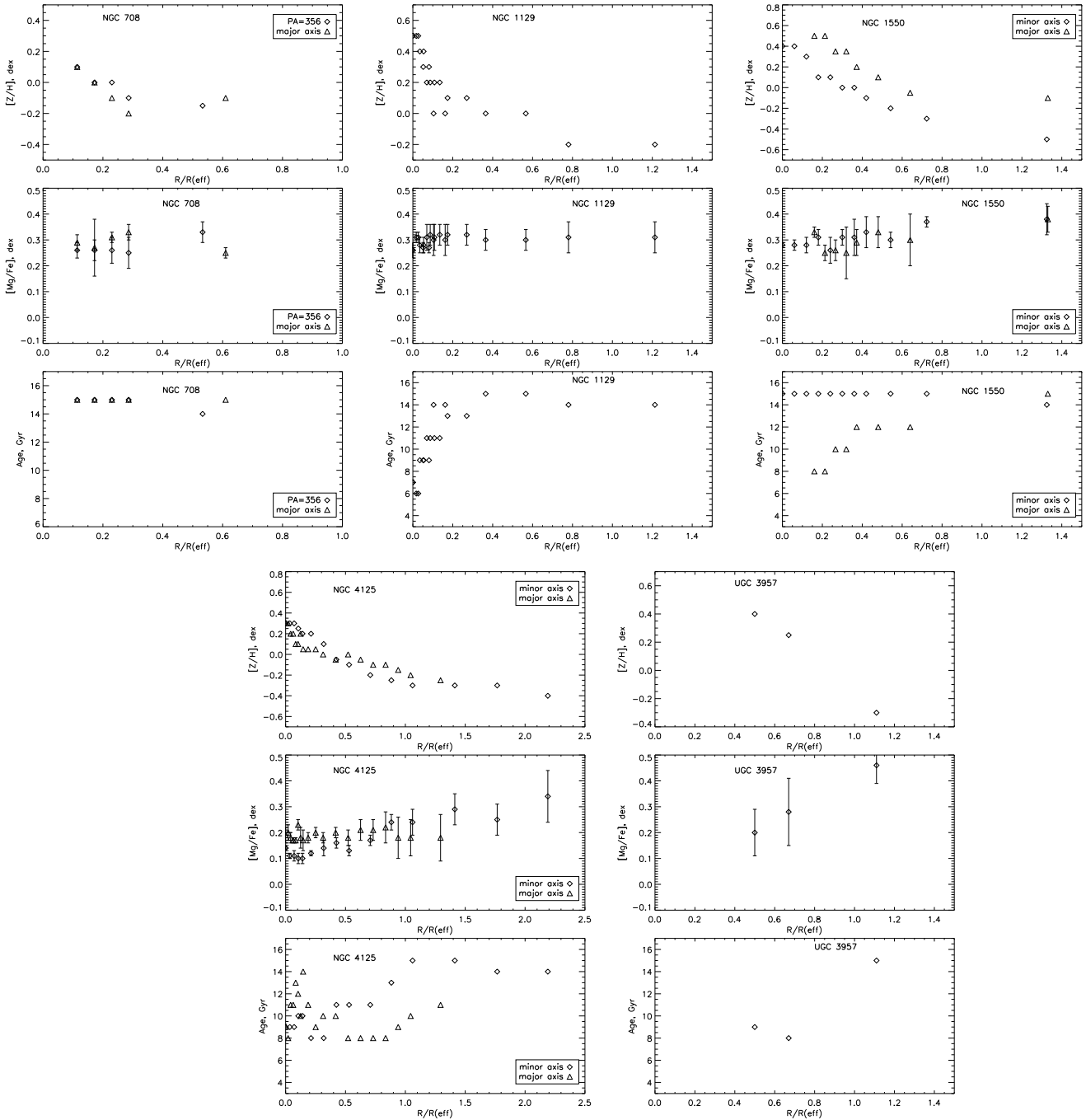


Figure 10. The radial variations of the stellar population parameters along the radius in five elliptical galaxies under consideration; in NGC 1129 both cross-sections are united since they give coincident dependencies.

using the model grid by Maraston (2005); the $[Z/H]$ and ages found from the Lick indices above have been used to select $M/L(V)$ corresponding to the stellar population properties at every radius. The radial profile of $M/L(V)$ for every galaxy is shown in Figure 11. The profiles are presented for the Kroupa IMF; if we prefer the classic Salpeter one, all the $M/L(V)$ values should be increased by a factor of 1.54

(found by confronting $M/L(V)$ for the Kroupa IMF with that for the Salpeter IMF calculated by Maraston 2005).

We have approximated the profiles of Figure 11 by smooth logarithmic or polynomial curves and have used the dependencies derived to transform the surface brightness profiles (this time, the surface brightness profiles obtained from the isophote analysis, with the corresponding

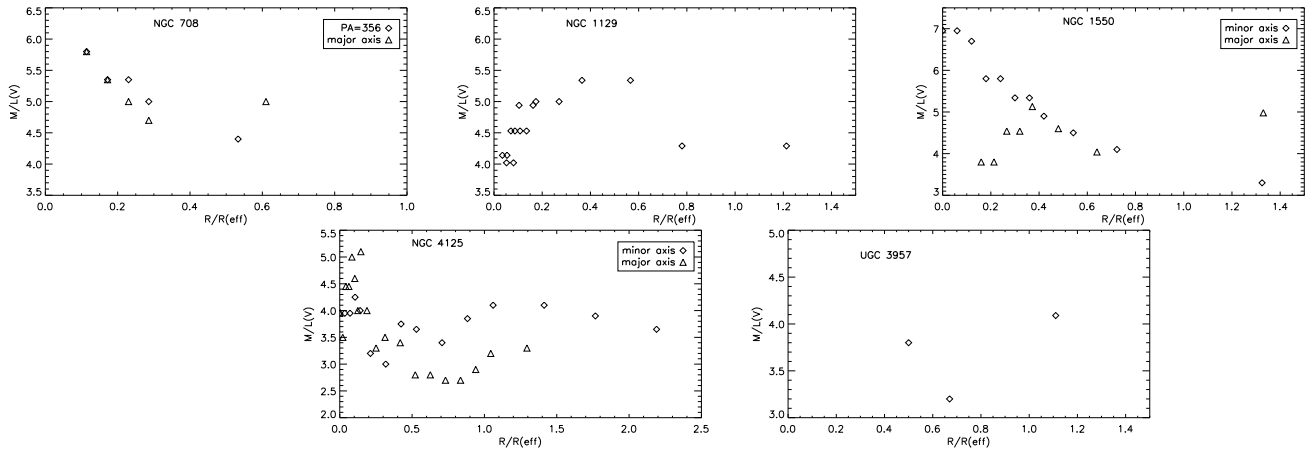


Figure 11. The variations of the stellar population mass-to-light ratios along the radius in five elliptical galaxies under consideration; in NGC 1129 both cross-sections are united since they give coincident dependencies.

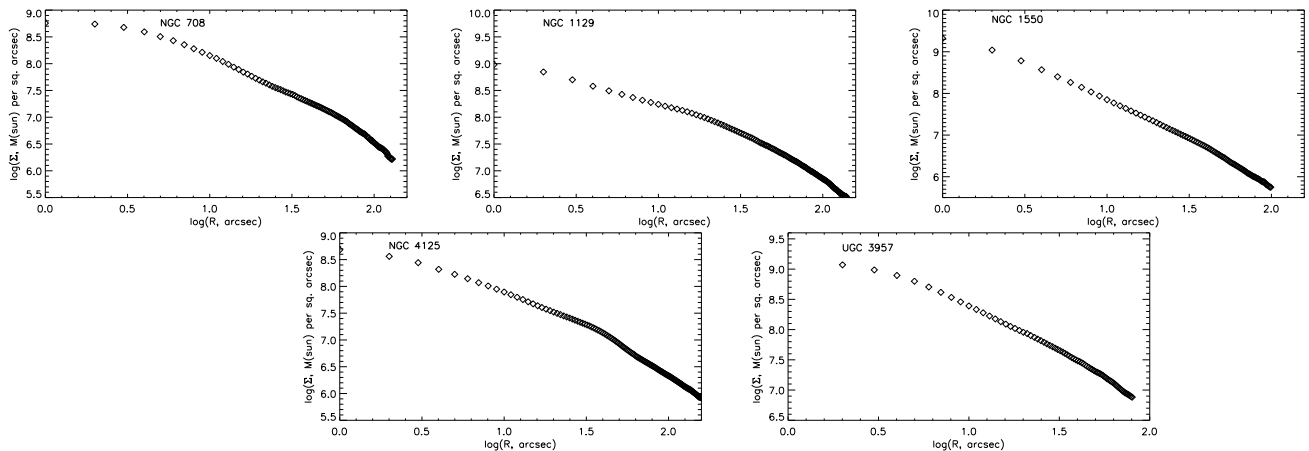


Figure 12. The radial profiles of the surface **mass** density along the radius in five elliptical galaxies under consideration.

azimuthally averaged values of R_{eff} into surface mass density profiles (Figure 12). Our aim was to estimate, though under very simple assumptions, the stellar mass which is contained within the radii R_{sweet} , to compare it with the dynamical masses derived in previous subsections. The profiles of Figure 12 were then deprojected with the formulae invented by Kholopov (1949), and after that we have integrated the volume mass density profiles up to R_{sweet} under the assumption of spherical symmetry. It is obvious that the assumption of spherical symmetry is very rude for our objects, especially for NGC 708 and NGC 4125, and the fact that the surface mass density profiles are not going to infinity but are cut at arbitrary radii provides only lower limits of the stellar mass estimates, however some feeling of the dark matter fraction within the optical borders of the giant elliptical galaxies can be obtained.

As we can see in Table 5, there is a range of dark mass presence among our small sample. In particular, NGC 4125 has the most of all its mass in stars. However, if we refer to

the Salpeter IMF, a typical fraction of dark matter within R_{sweet} is 60%. For the Kroupa IMF the sample averaged fraction is $\sim 75\%$. The comparison between the stellar and dynamical mass estimates measured within R_{sweet} is shown in Figure 13 (right panel).

4 DISCUSSION

We discuss one simple and fast, but nevertheless reliable method for estimating masses of early-type galaxies from the stellar surface brightness and the line-of-sight velocity dispersion profiles only. The method is based on the ansatz that the relation between the projected velocity dispersion and the circular speed is almost insensitive to the anisotropy of stellar orbits at a characteristic radius R_{sweet} where derived circular speed profiles for isotropic distribution of stars, pure circular and pure radial stellar orbits are close to each other. R_{sweet} lies close to the radius R_2 where the surface brightness

Table 5. Stellar masses ($V_c^* = \sqrt{\frac{GM_*(< R_{\text{sweet}})}{R_{\text{sweet}}}}$) and the fraction of dark matter within R_{sweet} for the Kroupa and Salpeter IMFs.

Galaxy	Kroupa IMF		Salpeter IMF	
	V_c^* , km s ⁻¹	% of dark matter	V_c^* , km s ⁻¹	% of dark matter
NGC 0708	178	77	221	64
NGC 1129	218	76	270	63
NGC 1550	190	75	236	62
NGC 4125	248	56	308	32
UGC 3957	174	87	216	79

Table 6. Ellipticity and effective radius for the sample galaxies. The columns are: (1) - galaxy name; (2) - ellipticity; (3) - effective radius defined from the de Vaucouleurs fit to the ellipse-averaged surface brightness profile; (4) - effective radius defined from the de Vaucouleurs fit to the long-slit profile.

Name (1)	Ellipticity (2)	R_{eff} , arcsec (3)	$R_{\text{eff}}^{\text{slit}}$, arcsec (4)
NGC 708	0.45	63.5 ± 1.5	58.4 ± 2.9
NGC 1129	0.22	86.7 ± 2.4	61.7 ± 6.8
NGC 1550	0.11	25.7 ± 0.7	18.5 ± 1.1
NGC 4125	0.46	56.4 ± 0.4	54.3 ± 0.7
UGC 3957	0.1	33.9 ± 0.8	22.1 ± 1.0

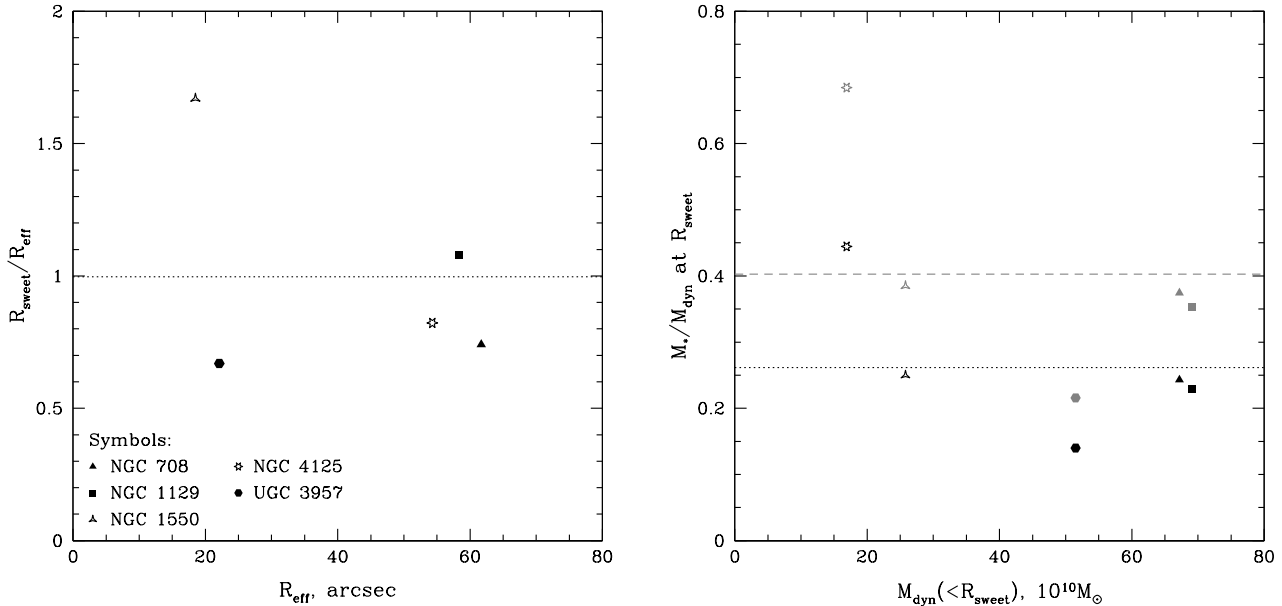


Figure 13. Left: the comparison between the sweet radius R_{sweet} and the effective radius $R_{\text{eff}}^{\text{slit}}$, defined from the de Vaucouleurs fit to the long-slit surface brightness profile. Different symbols denote different galaxies: the solid triangle - NGC 708, the solid square - NGC 1129, the curved triangle - NGC 1550, the star - NGC 4125, the solid hexagon - UGC 3957. The dotted line shows to average ratio $R_{\text{sweet}}/R_{\text{eff}}^{\text{slit}}$. Right: the comparison between the stellar $M_*(< R_{\text{sweet}})$ and dynamical $M_{\text{dyn}}(< R_{\text{sweet}}) = [V_c^{\text{iso}}]^2 R_{\text{sweet}}/G$ mass at the sweet radius. Black symbols show the ratio M_*/M_{dyn} for the Kroupa IMF and grey symbols - for the Salpeter IMF. The black dotted and grey dashed lines indicate the average ratio M_*/M_{dyn} for the Kroupa and Salpeter IMFs, respectively.

$I(R)$ declines as R^{-2} , which is in turn not far from the effective radius of the galaxy R_{eff} . Although the method allows to estimate mass within some particular radius only (or in radial range where $I(R) \propto R^{-2}$), it does not require any a priori parametrization of mass or anisotropy profiles and the resulting estimate does not depend significantly on the quality of data. The method has already been tested on a sample of 65 simulated galaxies drawn from cosmological simulations by Oser et al. (2010) in Lyskova et al. (2012). When averaged over the subsample of massive ($\sigma_p(R_{\text{eff}}) > 150 \text{ km s}^{-1}$) slowly rotating galaxies the recovered circular speed is almost unbiased ($\overline{\Delta_{\text{opt}}} < 1\%$) with modest scatter (RMS = 5.4 %). Note that in Lyskova et al. (2012) the surface brightness and the line-of-sight velocity dispersion profiles were calculated in a set of logarithmic concentric annuli around the center of the simulated galaxy. In this paper we (i) mimic the long-slit observations by computing the profiles along the slits, and also (ii) extend our analysis to rotating elliptical galaxies by considering $V_{\text{rms}}(R) = \sqrt{\sigma_p^2(R) + V_{\text{rot}}^2(R)}$ instead of $\sigma_p(R)$ in equations (4) or (6), where $V_{\text{rot}}(R)$ is the observed rotational velocity. Tests have been performed on the sample of massive simulated galaxies ($\sigma_p(R_{\text{eff}}) > 150 \text{ km s}^{-1}$, edge-on view) that includes both fast and slow rotators in proportion close to the observed one reported by ATLAS^{3d} team (Emsellem et al. 2007). We find that the circular speed recovered from $I(R)$ and $\sigma_p(R)$ measured along the slit aligned with the apparent major axis of the galaxy is on average underestimated by 4–5% and the RMS-scatter is about 6%. The bias almost vanishes when $\sigma_p(R)$ in equations (4) is substituted with $V_{\text{rms}}(R) = \sqrt{\sigma_p^2(R) + V_{\text{rot}}^2(R)}$ and the RMS-scatter remains the same. If profiles are measured along apparent major and minor axes of the galaxy then we can reduce the scatter arising from triaxiality of elliptical galaxies. Indeed, in this case the RMS-scatter is reduced down to 5%.

X-ray circular speed profiles for all galaxies are inferred under an assumption of constant metallicity ($Z = 0.5Z_{\odot}$), although the errorbars are estimated in a conservative way, allowing for the abundance gradients. If the abundance steadily increases to the galaxy center, then the assumption of the flat metallicity profile would lead to overestimated circular velocity. The decreasing at small radii abundance would imply instead that V_c^X is underestimated. Abundance measurements for low temperature ($\lesssim 1.5 \text{ keV}$) systems remains among the most important uncertainties in X-ray determination of the circular speed of elliptical galaxies. For hotter systems the impact of abundance is much less severe. For instance, the conservative estimate for NGC0708 suggests that the circular speed may be over-/underestimated as much as 25-30 % (at $R \lesssim 30 - 40''$).

The inferred circular speed estimates from optical data and from X-ray for all galaxies in our sample agree with each other remarkably well, especially for NGC 1550 and NGC 1129, indicating the relaxed dynamical state of these galaxies, close to isotropic distribution of stellar orbits within 1-2 effective radii and that hot gas in these objects is in the hydrostatic equilibrium. The only rotating galaxy in our sample, NGC 4125, is also the only galaxy with non-negligible

nonthermal pressure support (at the level of $\approx 36\%$). For UGC 3957 both X-ray and optical methods give the same (within errorbars) result at the sweet point and at larger radii we observe that $V_c^X(R) > V_c^{\text{iso}}(R)$ what may be interpreted as the radially biased stellar velocity anisotropy. NGC 708 is the most difficult galaxy for interpretation. At $R \lesssim 30''$ where optical data are quite reliable $V_c^X(R)$ lies below $V_c^{\text{iso}}(R)$. Then at $30'' \gtrsim R \gtrsim 60''$ these two curves are roughly consistent with each other. At the sweet spot which is located slightly beyond the radial range with available optical data the X-ray mass estimate exceeds the optical one by $\sim 40\%$ although the reliability of the V_c^{iso} at this radius is under question and errorbars are quite large. The average ratio between the optical V_c^{iso} and V_c^X at the sweet spot is equal to 0.98 with ≈ 0.11 rms-scatter⁶. Given the scatter, this result indicates that on average the non-thermal contribution to the total gas pressure is consistent with zero. Two galaxies - NGC 4125 and NGC 0708 - that have the lowest central velocity dispersions and are showing the largest deviation of $\left\langle \frac{V_c^{\text{iso}}}{V_c^X} \right\rangle$ from the mean value, appear to be especially prone to abundance uncertainties in X-ray analysis. Low temperature of NGC 4125 ($T \approx 0.5 \text{ keV}$) does not allow to disentangle reliably continuum and emission lines. In its turn, NGC 0708 has higher temperature at the sweet radius ($\approx 1.7 \text{ keV}$) but shows significant abundance gradients, what leads to large spread in the resulting circular velocity curves. If we exclude these two galaxies, then the average ratio is $\left\langle \frac{V_c^{\text{iso}}}{V_c^X} \right\rangle \approx 0.96$ with $RMS \approx 0.03$. This scatter is comparable to the expected value of 5.4% coming from the analysis of a sample of simulated massive elliptical galaxies without significant rotation (Lyskova et al. 2012).

It should be mentioned that for our analysis we deliberately use the surface brightness profiles measured along the slit rather than ellipse-averaged radial profiles. On one hand, $I(R)$ along specific PA could be affected by local inhomogeneities in brightness and the signal-to-noise ratio is smaller compared to azimuthally-averaged profiles. On the other hand, analysing the projected velocity dispersion and surface brightness profiles measured in the same way seems to be more self-consistent and justified. Moreover, we aim to demonstrate performance of our simple mass estimator using the most basic observables, thus on purpose neglecting all possible complications. Apart from using the original surface brightness distribution along the specific PA, we also simplify the analysis by neglecting departures from spherical symmetry (see eq. 9-11). If we take into account information on ellipse-averaged radial profiles and ellipticity of a given galaxy, we will get the V_c -estimate similar to the reported one (within errorbars), although the averaged surface profiles are slightly shallower than original ones pushing R_{sweet} towards larger radii where kinematics is getting less reliable.

The full version of analysis, i.e. equations (4), is recommended to use when the projected velocity dispersion profile is reliable over the radial range of interest. As the

⁶ $\bar{x} = \frac{\sum x}{N} \pm \frac{RMS}{\sqrt{N}}$, $RMS = \sqrt{\frac{\sum (x-\bar{x})^2}{N}}$

circular speed $V_c^{\text{rad}}(R)$ recovered for pure radial orbits depends on the second derivative $\delta = \frac{d^2 \ln[I(R)\sigma_p^2(R)]}{d(\ln R)^2}$, it relies on the quality of $\sigma_p(R)$. If the dispersion profile is noisy and does not decline steeply, then R_2 - the radius where $\alpha = d \ln I(R)/d \ln R = 2$ - can be used as the sweet spot. For our sample of galaxies the average ratio $\left\langle \frac{V_c^{\text{iso}}(R_{\text{sweet}})}{V_c^{\text{iso}}(R_2)} \right\rangle$ of circular speed estimates calculated from equations (4) at R_{sweet} and at R_2 is equal to 1.02 with $RMS = 0.016$. When the observational data do not allow to use the full analysis, then the circular speed can be estimated using the simplified analysis (eq. 6). The average ratio $\left\langle \frac{V_c^{\text{iso}}(R_{\text{sweet}})}{V_c^{\text{iso},s}(R_2)} \right\rangle$ equals to 1.04 with $RMS = 0.032$, where $V_c^{\text{iso},s}$ is calculated using equations (6).

As expected the sweet radius is found to lie close to R_2 and also not far from the effective radius R_{eff} of a galaxy (effective radii used here, $R_{\text{eff}}^{\text{slit}}$ are listed in Table 6). For our sample the average ratio $\left\langle \frac{R_{\text{sweet}}}{R_2} \right\rangle \approx 1.06$ with rms-scatter $RMS \approx 15\%$, while $\left\langle \frac{R_{\text{sweet}}}{R_{\text{eff}}^{\text{slit}}} \right\rangle \approx 1.0$ with $RMS \approx 36\%$ scatter. The ratio $\frac{R_{\text{sweet}}}{R_{\text{eff}}^{\text{slit}}}$ as a function of $R_{\text{eff}}^{\text{slit}}$ is shown in Figure 13 (left panel). For successful implementation of our simple estimator the surface brightness and kinematic profiles should extend slightly beyond R_{sweet} or R_2 as equations (4) require differentiation of the observed profiles. For Sérsic surface brightness distribution $I(R) = I(R_{\text{eff}}) \exp \left[-b_n \left((R/R_{\text{eff}})^{1/n} - 1 \right) \right]$, where $b_n \simeq 2n - 0.324$ (for $0.5 \leq n \leq 10$, Ciotti 1991), R_2 is related to R_{eff} via (Graham and Driver 2005)

$$R_2 \simeq \left(\frac{2n}{b_n} \right)^n R_{\text{eff}} \simeq 1.2 R_{\text{eff}}, \quad (12)$$

i.e. $R_2 \simeq 1.2 R_{\text{eff}}$. So in terms of effective radii the observed profiles should extend out to $\sim 1.2 - 1.5 R_{\text{eff}}$ for reliable mass determination. It should be noted that the value of the effective radius strongly depends on a measurement technique. The effective radii R_{eff} and $R_{\text{eff}}^{\text{slit}}$ for our sample galaxies obtained from the de Vaucouleurs fit to the ellipse-averaged and long-slit surface brightness profiles correspondingly are listed in Table 6. For some galaxies R_{eff} and $R_{\text{eff}}^{\text{slit}}$ are different by a factor of ~ 1.5 . The effective radius could vary significantly depending on (i) whether it is measured with or without extrapolation of data, (ii) parametric form of the stellar distribution profile used to fit the data, (iii) radial range used to fit, for instance, the Sérsic profile, (iv) quality of photometric data (see, e.g., Kormendy et al. 2009; Cappellari et al. 2013). In contrast with the simple mass estimator proposed by Wolf et al. (2010) our estimator is not tied to the effective radius. The sweet spot is defined from *local* properties of $I(R)$ and $\sigma_p(R)$ or even from $I(R)$ alone.

5 CONCLUSION

We discuss a simple mass estimator that allows one to estimate the circular speed V_c from *local* properties of the surface brightness and the line-of-sight kinematics at a characteristic radius where the V_c -estimate is largely insensitive to the unknown anisotropy of stellar orbits. Although the method is designed for non-rotating spherical galaxies, we extend it also to mildly rotating axisymmetric and slowly-rotating triaxial ones, substituting $\sigma_p(R)$ in equation 4 or 6 with $V_{\text{rms}}(R) = \sqrt{\sigma_p^2(R) + V_{\text{rot}}^2(R)}$, where $V_{\text{rot}}(R)$ is the rotational velocity. Tests on the sample of massive simulated galaxies show that the recovered from $I(R)$ and $\sigma_p(R)$ measured along apparent major and minor axes of the galaxy circular speed is almost unbiased with the RMS-scatter of $\sim 5\%$.

We apply the method to M87 and compare our simple mass estimate with circular speed profiles derived from X-rays and the state-of-the-art Schwarzschild modeling, thus revisiting the results of Churazov et al. (2008, 2010). At the sweet radius $R_{\text{sweet}} = 141''$ we derive $V_c^{\text{opt}} = 524 \text{ km s}^{-1}$, that agrees well with the circular speed obtained in Murphy et al. (2011). After comparing the optical V_c -estimate with the X-ray derived one, we conclude that at the sweet radius the non-thermal contribution to the total gas pressure is $\sim 25\%$. The true value of the non-thermal contribution in M87 could be even lower, since X-ray data near the sweet radius are affected by the shock (Forman et al. 2007).

We observe a sample of five X-ray bright elliptical galaxies with the 6-m telescope of the SAO RAS and measure the surface brightness, line-of-sight velocity and velocity dispersion distribution of stars up to two effective radii along one or two slits. We apply our simple method to estimate the circular speed and compare it with the circular speed measurements based on the X-ray analysis of Chandra data. We conclude that optical and X-ray V_c -estimates agree with each other remarkably well implying the sample averaged non-thermal pressure support of $\sim 4\% \pm 20\%$, i.e. to be consistent with zero.

From deep long-slit spectral data obtained with SCORPIO/BTA we derive high-precision Lick indices profiles out to ~ 2 effective radii, which in turn used to estimate the radial variations of the stellar population mass-to-light ratios and the dark matter fraction within R_{sweet} , typical value of the latter is $\sim 60\%$ for the Salpeter IMF and $\sim 75\%$ for the Kroupa IMF.

6 ACKNOWLEDGMENTS

We are grateful to the referee for very useful comments and suggestions. NL is grateful to the International Max Planck Research School on Astrophysics (IMPRS) for financial support. NL acknowledges Scott Tremaine and Thorsten Naab for helpful discussions and Jeremy Murphy for providing kinematic profiles for M87. This research has made use of the NED which is operated by the Jet Propulsion Laboratory, California Institute of Technology, under contract with the National Aeronautics and Space Administration.

This work was partly supported by the Research Program OFN-17 of the Division of Physics, Russian Academy of Sciences, and by the Program of State Support for Leading Scientific Schools of the Russian Federation (grant no. NSH-6137.2014.2). AM is also grateful for the financial support of the ‘Dynasty’ Foundation. We thank Azamat Valeev, Timur Fatkhullin and Alexander Vinokurov for supporting the SCORPIO observations, and especially Victor Afanasiev for his great contribution to spectroscopy at the 6 m telescope.

REFERENCES

- Afanasiev V. L., Moiseev A. V. 2005, *Astron. Letters*, 31, 194
- Afanasiev V. L., Moiseev A. V. 2011, *Baltic Astronomy*, 20, 363
- Anders E., Grevesse N. 1989, *Geochim. Cosmochim. Acta*, 53, 197
- Arnaud K. A. 1996, *Astronomical Data Analysis Software and Systems V*, 101, 17
- Baes M., Sil’chenko O. K., Moiseev A. V., Manakova E. A. 2007, *A&A*, 467, 991
- Bell E. F., McIntosh D. H., Katz N., Weinberg M. D. 2003, *ApJ Suppl Ser*, 149, 289
- Buote D. A. 2000, *MNRAS*, 311, 176
- Buote D. A., Humphrey P. J. 2012, in Kim D.-W., Pellegrini S., eds, *Astrophysics Space Science Library Vol. 378, Hot Interstellar Matter in Elliptical Galaxies*. Springer, Berlin, p. 235
- Buote D. A., Humphrey P. J. 2012, *MNRAS*, 421, 1399
- Cappellari M. et al. 2013, *MNRAS*, 432, 1709 (Paper XV)
- Ciotti L. 1991, *A&A*, 249, 99
- Churazov E., Forman W., Jones C., Böhringer H. 2003, *ApJ*, 590, 225
- Churazov E., Forman W., Vikhlinin A., Tremaine S., Gerhard O., Jones C. 2008, *MNRAS*, 388, 1062
- Churazov E., Tremaine S., Forman W., Gerhard O., Das P., Vikhlinin A., Jones C., Böhringer H., Gebhardt K. 2010, *MNRAS*, 404, 1165
- Coccatto L., Gerhard O., Arnaboldi M. 2010, *MNRAS Letters*, 407, L26
- Côté P., McLaughlin D.E., Hanes D.A., Bridges T.J., Geisler D., Merritt D., Hesser J.E., Harris G.L.H., Lee M.G. 2001, *ApJ*, 559, 828
- de Lucia G., Blaizot J. 2007, *MNRAS*, 375, 2
- Dickey J. M., Lockman F. J. 1990, *ARAA*, 28,215
- Emsellem E., Cappellari M., Peletier R. F., McDermid R. M., Bacon R., Bureau M., Copin Y., Davies R. L., Krajnović D., Kuntschner H., Miller B.W., de Zeeuw P.T. 2004, *MNRAS*, 352, 721
- Emsellem E., Cappellari M., Krajnović D., van de Ven G., Bacon R., Bureau M., Davies R. L., de Zeeuw P. T., Falcón-Barroso J., Kuntschner H., McDermid R., Peletier R. F., Sarzi M. 2007, *MNRAS*, 379, 401
- Emsellem E., Cappellari M., Krajnović D., Alatalo K., Blitz L., Bois M., Bournaud F., Bureau M., Davies R. L., Davis T. A., de Zeeuw P. T., Khochfar S., Kuntschner H., Lablanche P.-Y., McDermid R. M., Morganti R., Naab T., Oosterloo T., Sarzi M., Scott N., Serra P., van de Ven G., Weijmans A.-M., Young L. M. 2011, *MNRAS*, 414, 888
- Forman W., Jones C., Tucker W. 1985, *ApJ*, 293, 102
- Forman W., Jones C., Churazov E., Markevitch M., Nulsen P., Vikhlinin A., Begelman M., Böhringer H., Eilek J., Heinz S., Kraft R., Owen F., Pahre M. 2007, *ApJ*, 665, 1057
- Fukazawa Y., Botoya-Nonesa J. G., Pu J., Ohto A., Kawano N. 2006, *AJ*, 636, 698
- Gebhardt K., Richstone D., Kormendy J., Lauer T.R., Ajhar E.A., Bender R., Dressler A., Faber S. M., Grillmair C., Magorrian J., Tremaine S. 2000, *AJ*, 119, 1157
- Gebhardt K., Richstone D., Tremaine S., Lauer T.R., Bender R., Bower G., Dressler A., Faber S. M., Filippenko A.V., Green R., Grillmair C., Ho L.C., Kormendy J., Magorrian J., Pinkney J. 2003, *ApJ*, 583, 92
- Gebhardt K., Thomas J. 2009, *ApJ*, 700, 1690
- Gerhard O.E. 1993, *MNRAS*, 265, 213
- Gerhard O., Kronawitter A., Saglia R. P., Bender R. 2001, *AJ*, 121, 1936
- Graham A.W., Driver S.P. 2005, *Publications of the Astronomical Society of Australia*, 22, 118
- Humphrey P. J., Buote D. A. 2006, *ApJ* 639, 136
- Johnson R., Chakrabarty D., O’Sullivan E., Raychaudhury S. 2009, *ApJ*, 706, 980
- Kholopov P. N. 1949, *AZh*, 26, 298
- Kobayashi C. 2004, *MNRAS*, 347, 740
- Koopmans L. V. E., Treu T., Bolton A. S., Burles S., Moustakas L. A. 2006, *ApJ*, 649, 599
- Kormendy J., Fisher D. B., Cornell M. E., Bender R. 2009, *ApJS*, 182, 216
- Lau E. T., Kravtsov A. V., Nagai D. 2009, *ApJ*, 705, 1129
- Lyskova N., Churazov E., Zhuravleva I., Naab T., Oser L., Gerhard O., Wu X. 2012, *MNRAS* 423, 1813
- Mamon G.A. and Boué G. 2010, *MNRAS*, 401, 2433
- Maraston C. 2005, *MNRAS*, 362, 799
- McLaughlin D.E. 1999, *AJ*, 117, 2398
- Moiseev A.V. 2001, *Bull. SAO.*, 51, 11 (astro-ph/0111219)
- Murphy J. D., Gebhardt K., Adams J. J. 2011, *ApJ*, 729, 129
- Naab T., Johansson P. H., Ostriker J. P., Efstathiou G. 2007, *ApJ*, 658, 710
- Naab T., Oser L., Emsellem E., Cappellari M., Krajnović, McDermid R.M., Alatalo K., Bayet E., Blitz L., Bois M., Bournaud F., Bureau M., Crocker A., Davies R.L., Davis T.A., de Zeeuw P.T., Duc P.-A., Hirschmann M., Johansson P.H., Khochfar S., Kuntschner H., Morganti R., Oosterloo T., Sarzi M., Scott N., Serra P., van de Ven G., Weijmans A., Young L.M. *MNRAS*, submitted
- Nagai D., Vikhlinin A., Kravtsov A. V. 2007, *ApJ*, 655 98
- Oser L., Ostriker J.P., Naab T., Johansson P.H., Burkert A. 2010, *ApJ*, 725, 2312
- Percival S. M., Salaris M., Cassisi S., Pietrinferni A. 2009, *ApJ*, 690, 427
- Piffaretti R., Jetzer Ph., Schindler S. 2003, *AA*, 398, 41
- Pu S. B., Saglia R. P., Fabricius M. H., Thomas J., Bender R., Han Z. 2010, *A&A*, 516, A4
- Richstone D. O., Tremaine S. 1984, *ApJ* 286, 27
- Romanowsky A. J., Kochanek C. S. 2001, *ApJ*, 553, 722

- Rusli S. P., Thomas J., Erwin P., Saglia R. P., Nowak N., Bender R. 2011, MNRAS, 410, 1223
- Schwarzschild M. 1979, ApJ, 232, 236
- Shen J., Gebhardt K. 2010, ApJ, 711, 484
- Sil'chenko O. K., Moiseev A. V., & Shulga, A. P. 2010, AJ, 140, 1462
- Smith R.K., Brickhouse N.S., Liedahl D.A., Raymond J.C. 2001, ApJ, 556, L91
- Thomas D., Maraston C., Bender R. 2003, MNRAS, 339, 897
- Thomas J., Saglia R.P., Bender R., Thomas D., Gebhardt K., Magorrian J., Richstone D. 2004, MNRAS, 353, 391
- Thomas J., Saglia R.P., Bender R., Thomas D., Gebhardt K., Magorrian J., Corsini E.M., Wegner J. 2005, MNRAS, 360, 1355
- Thomas J., Jesseit R., Naab T., Saglia R. P., Burkert A., Bender R. 2007, MNRAS, 381, 1672
- Trager S. C., Faber S. M., Worthey G., González J. J. 2000, AJ, 120, 165
- Treu T., Koopmans L. V., Bolton A. S., Burles S., Moustakas L. A. 2006, ApJ, 640, 662
- van der Marel R.P. 1994, MNRAS, 270, 271
- Vikhlinin A., Markevitch M., Murray S.S., Jones C., Forman W., Van Speybroeck L. 2005, ApJ, 628, 655
- Wegner G. A., Corsini E. M., Thomas J., Saglia R. P., Bender R., Pu S. B. 2012, AJ, 144, A78
- Wolf J., Martinez G.D., Bullock J.S., Kaplinghat M., Geha M., Muñoz R.R., Simon J.D., Avedo F.F. 2010, MNRAS, 406, 1220
- Wu X., Gerhard O., Naab T., Oser L., Martinez-Valpuesta I., Hilz M., Churazov E., Lyskova N. MNRAS, submitted
- Zhuravleva I., Churazov E., Kravtsov A., Lau E. T., Nagai D., Sunyaev R. 2013, MNRAS, 428, 3274